The Dissertation Committee for Benjamin Thomas Bowes

certifies that this is the approved version of the following dissertation:

Energy transport in high temperature, high density plasmas on femtosecond timescales.

Committee:

Michael Downer, Supervisor

Todd Ditmire

Charles Chiu

Manfred Fink

John Keto

Michael Becker

Energy transport in high temperature, high density plasmas on femtosecond timescales.

by

Benjamin Thomas Bowes, B.S.

Dissertation

Presented to the Faculty of the Graduate School of

The University of Texas at Austin

in Partial Fulfillment

of the Requirements

for the Degree of

Doctor of Philosophy

The University of Texas at Austin

May 2007

To my loving family.

Acknowledgments

There are many great, wonderful people that helped me over the years. Thank you to my lab mates in Austin: Rafal Zgadzaj, Bonggu Shim, Jinhee Kwon, Ramon Carriles-Jaimes, Peter Figliozzi, Liang Feng Sun, Peng Dong, Nicholas Matlis, PJ Smith and Franklin Grigsby. Thank you to my friends for keeping me sane: Nathan Harrison, David Stoker, Irina Churina, V. Reid Smith, Greg Deist, Melanie Kittle, Laura Feeney, Carl Knutson, Jenny Sobeck, Ned Flagg, Becky Thompson-Flagg, Jenn Kreft, Flip Kromer, Sonia Kumar, Cindy Stowell, Jason Hess, Chris Wieland, Tiffany Mabee, Jerry Schirmer, Jo Tschetter, Will Grigsby, Emily Grigsby, Gilliss Dyer, Phil Janisiewicz, and Greg Hays. Prof. Hans Langhoff, thank you for teaching me about radiative diffusion. James Halligan made purchasing fast and easy. Cathy Rapinett made travel planning understandable. Super Big Hugs to my Ann Arbor friends Yanwen Wu and Jonathan Farrugia. Thanks to Bixue Hou, James Easter, Marc Wilcox, Peter Diehr and John Nees for friendship, help and conversation while in Ann Arbor. Much love to my parents, Kerry and Thomas Bowes, and my sister, Katie Bowes, for being with me this entire journey. Thanks to Andy Crouch for teaching me the value of obviousness. Thank you Mike Downer for pushing me to be a better scientist. And, thank you Jane Downer for making tasty cookies.

This work has been supported by National Science Foundation FOCUS grant 0114336, Department of Energy grant DE-FG03-96ER40954, and National Nuclear Security Administration Stewardship Science Academic Alliances cooperative agree-

ment DE-FC52-03NA00156.

Benjamin Thomas Bowes

The University of Texas at Austin

May 2007

Energy transport in high temperature, high density plasmas on femtosecond timescales.

Publication No. _____

Benjamin Thomas Bowes, Ph.D.
The University of Texas at Austin, 2007

Supervisor: Michael Downer

In this work we apply femtosecond (fs) microscopy to a solid target (aluminum and copper) irradiated at relativistic intensity ($I_{pu} \geq 2 \times 10^{18}$ W/cm^2) by high-contrast ($\geq 1 : 10^{-9}$), obliquely-incident ($\theta_{pu}^{inc} = 45°$), P- and S-polarized pump pulses ($\lambda_{pu} = 0.8$ μm, 35 fs) focused to a *wavelength-scale* spot size ($w_0 = 0.8$ μm). Under these conditions, radiation and hot electrons are the dominant carriers of energy out of the initially photo-excited volume. The mean free paths governing both transport processes exceed the spot size w_0, opening the study of ballistic transport of energy into surrounding target material. This femtosecond microscopy experiment, with λ_{pu}^2 pump spot, is well-suited to observe the initial stages, and the radial dimension, of such non-local transport directly on any target material. The physics of this

transport is relevant to fast ignition of laser fusion, to generation of ultrashort pulsed x-rays and relativistic proton and ion beams, and to astrophysics. The experimental interaction volume may be small enough that the entire experiment is amenable to large-scale particle-in-cell simulations.

Contents

List of Tables

List of Figures

Chapter 1

Introduction

With the advent of short-pulse, high-peak-power laser systems, whole new regimes of physics have been opened up to scientists. The areas opened up are the studies of dynamic processes over timescales of a few picoseconds to a few femtoseconds, the behavior of matter under conditions of high pressure ($>$ 500 kbar), high temperature ($>$ 10 eV) and high density ($> 10^{19}$ cm^{-3}). In particular, the problems of fast ignition of fusion plasmas, energy transport for astrophysical systems, and generation of short pulse x rays are of interest.

Knowing how to optimize and control the production of hot electrons in laser-plasma experiments is important for use in fast-ignition of laser fusion plasmas. [1, 2, 3, 4, 5, 6] In these experiments a gold cone is heated by an intense, short laser pulse. Hot electrons ($T_{e,hot} \geq 1$ keV) are created during the interaction of the laser pulse with the material. The electrons are confined to move along the surface of the gold cone by self-generated magnetic fields. [7, 8, 9, 10, 11, 12] At the tip of the cone is a compressed fusion pellet. Energy carried by the hot electrons is deposited in this compressed material igniting the fusion process. For these types of experiments

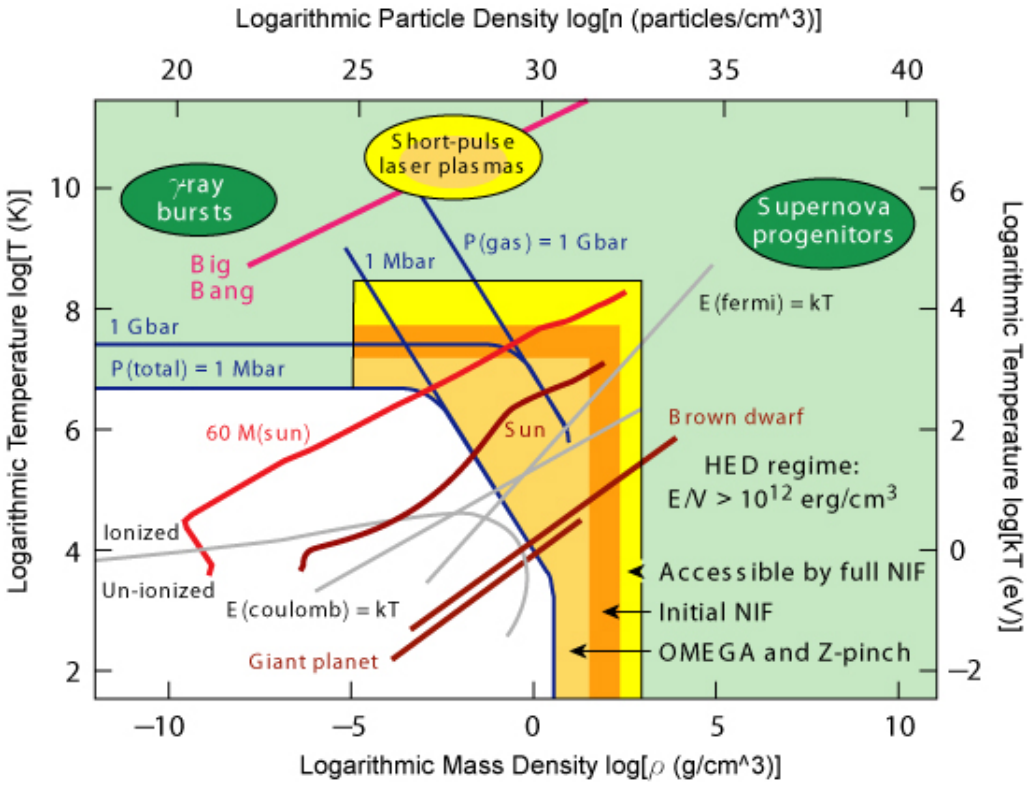

Figure 1.1: Temperature and pressure (parameter) regimes for plasma systems of astrophysical interest and systems accessible with current short pulse laser technology. [Adapted from NRC Report "Frontiers in High Energy Density Physics" and R. P. Drake, *High-Energy-Density Physics*]

to be successful, it is important to control and tailor the number, peak energy, and energy spread of these electrons. [13, 14, 15] Since these experiments are typically performed on large scale, low repetition rate (typically < 0.1 Hz) laser systems it is economically and scientifically critical to diagnose the hot electron production with separate experiments with the use of smaller laser facilities.

Another area of current research interest is the engineering of short-pulse, micrometer-sized x ray sources for high resolution imaging. Such an x ray source would be very useful for imaging of modern electronic circuits, molecular dynamics and biological samples. A temporally short x ray pulse would limit exposure of the sample to damaging radiation while still providing a high quality "snap shot" of the sample. [16, 17, 18] High spatial resolution is very desirable to gain insight into the dynamics of molecules or microstructure of biological samples.

Optimizing and controlling the laser produced x ray source size depends on detailed understanding of the energy transport dynamics within the source microplasma. By understanding this physics, the researcher may vary the size of the microplasma and the timescale over which it grows. This allows for fine tuning of the x ray source size and the x ray pulse duration. [19, 20]

There are many areas of astrophysical interest, such as equations of state and material opacity, that involve a significant amount of energy transport physics in extremely dense ($n_e \geq$ solid material), extremely hot ($T_e \geq 1$ keV) plasmas. [21, 6] (see figure 1.1) Detailed models of such astrophysical systems require accurate knowledge of the radiative opacities of material under similar state conditions. [22] Only recently have high power femtosecond laser systems evolved to the point where laboratory tests of radiative opacity become practical. Through experiments such as those described in this dissertation scientists will be able to measure the radiative

opacity of a variety of materials across significant ranges of temperature and density. [23, 24, 25] This data may then be used to test, verify and extend analytical theories and computer simulations of exotic astrophysical systems. [5]

In this dissertation The Author will present and describe a series of experiments on high temperature, high density microplasmas, produced with high intensity kHz repetition rate femtosecond laser pulses. By exploiting the advantages of the λ^3 Laser system [26] and femtosecond microscopy [27] we have developed these niche experiments that can be applied to the scientific projects such as those described earlier. We will show that we observe energy transport via radiation and ballistic hot electrons in a micrometer-scale, solid density plasma. We have developed a 2-D diffusion model to analyze the radiative transport, and have collaborated with world experts for multidimensional particle-in-cell computer simulations of the hot electron transport.

Chapter 2

Experimental Setup

2.0.1 λ^3 Laboratory at the Center for Ultrafast Optical Science

The majority of experimental work done for this dissertation took place at the Center for Ultra-fast Optical Science (CUOS). CUOS is a research center dedicated exclusively to the development of new techniques for generating ultrashort and ultra intense laser pulses, and the application of these pulses to a variety of scientific and engineering problems. CUOS is part of the College of Engineering at the University of Michigan, Ann Arbor. This work took place as part of a large collaboration between the University of Texas at Austin and the University of Michigan called "Frontiers in Optical, Coherent and Ultrafast Science" (FOCUS).

λ^3 Laser System: Three different lasers

This work was done exclusively with the λ^3 Laser System. [26, 28] λ^3 is a high-repetition rate, femtosecond pulse laser system with high pulse contrast and excellent beam focusing parameters. During work on this dissertation, the λ^3 system went through three separate upgrades, each bringing a significant improvement over the

previous version. Without this highly compact, highly engineered and reliable laser system these experiments would not have been possible.

In its first incarnation, the λ^3 Laser system consisted of a FemtoSource femtosecond oscillator pumped by a long cavity Spectra-Physics Millennia V laser. The oscillator produced 25 fs pulses with about 40 nm bandwidth at 76 MHz repetition rate. A Pockels cell pulse picker reduced the laser repetition rate down to 400 Hz. This reduced beam was then spread out in time by a conventional optical stretcher and then amplified in a novel amplifier.

The amplifier was a Ti:sapphire multi-pass design. Rather than a traditional bow tie configuration, this amplifier made use of two 6 inch diameter spherical aluminum mirrors arranged in a confocal configuration on either side of the Ti:sapphire crystal. This configuration allowed the laser beam to maintain a small angle from the axis of the Ti:sapphire crystal, and helped keep beam abberations to a minimum. Optical pumping of the Ti:sapphire crystal is by a Spectra-Physics Evolution X laser. The laser pulse made 15 passes through the Ti:sapphire, amplifying it to an energy of approximately 2 mJ. The beam then was shuttered by another Pockels cell, and passed through a conventional optical compressor. This final Pockels cell helped to keep nanosecond scale laser pre-pulses to a minimum, improving the peak-to-pedestal contrast ratio. This system delivered 25 fs pulses, with energies up to 1 mJ on target with $1 : 10^{-5}$ contrast ratio.

To further improve the pulse contrast ratio, a pulse cleaner was installed between the pulse picker and the optical stretcher. The unstretched laser pulse was amplified by three passes through optically pumped Ti:sapphire and then passed through a saturable absorber (Schott IR85 glass). The saturable absorber suppresses most of the laser prepulses before allowing the main, intense laser pulse to pass

through. The cleaned pulse is then sent on to the optical stretcher. With this pulse cleaner system in place, the peak-to-pedestal contrast ratio of the system output is improved by approximately 20%.

In its final configuration, the λ^3 system was upgraded to a regenerative amplifier (regen) configuration with cryogenically cooled Ti:sapphire crystal. 1 inch diameter mirrors were used to form a cavity with round-trip time of about 35 ns. This combination of long cavity with small end mirrors helped to minimize amplified stimulated emission within the cavity, improving the pulse contrast ratio significantly over previous incarnations of this system.

By converting the laser system to a long cavity regenerative, cryo-cooled amplifier with small end mirrors, the pointing stability of the beam is dramatically improved. This is because the long cavity and small mirror configuration allows only very stable cavity modes to develop. Unstable modes will not survive more than a few passes in this laser cavity. Simultaneously with this upgrade, a second pump laser and Pockels cell were added to the system. The additional pump laser brings an approximately 3.5× increase to the laser energy. The additional Pockels cell, combined with high-quality polarizing optics, dramatically increases the pulse contrast ratio of the entire system to $1 : 10^{-11}$.

Another unique feature of the λ^3 laser system is the use of an adaptive optic as the final beam focusing element. On its path into the vacuum target chamber, the laser beam is bounced off of a deformable mirror. This mirror is a thin coating of aluminum on glass, mounted in front of 36 piezoelectric actuators. The actuators push and pull on the backside of the mirror, deforming it away from a planar surface profile. Although a perfectly flat surface profile is ideal for each mirror in the laser system, the ideal is not achievable in practice. Each optical element in the laser

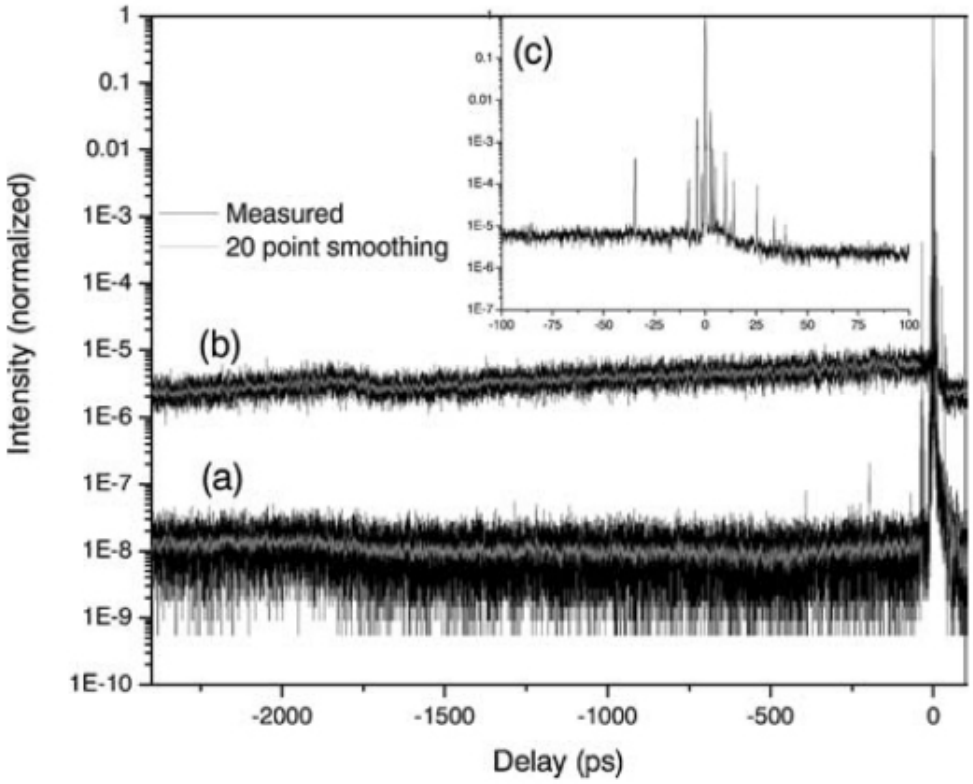

Figure 2.1: Contrast ratio measurement of the λ^3 laser system by third-order cross correlation. Curve (a) is the contrast of the entire system including the saturable absorber pulse cleaner. Curve (b) is without the saturable absorber pulse cleaner. Inset (c) zooms in around the main laser pulse to show more detail. There are 12 peaks in addition to the main pulse. Each of these peaks is due only to reflections within the cross correlator, not from actual laser pre-pulses. [Hong *et. al.*, Applied Physics B, **81**, 447 - 457 (2005)]

system deviates from an ideal shape and makes the laser beam 'ugly'. The final laser beam is substantially different from an ideal Gaussian spatial profile because of the cumulative effects of these distortions. The deformable mirror can be shaped to give a distortion to the beam that corrects for the cumulative distortions and returns the beam to an ideal Gaussian profile. The net result is a laser beam with a flat phase front and Gaussian spatial intensity distribution.

The beam correction process is handled by a learning ("genetic") algorithm. [26, 29] The final laser beam is focused onto a nonlinear optical crystal, producing a frequency doubled beam. This 2ω beam is filtered to remove residual fundamental light and imaged by a microscope objective onto a photodiode. The photodiode signal is averaged through a boxcar integrator and monitored by computer. The voltage of the photodiode signal is proportional to the intensity of the 2ω beam. The intensity of the 2ω beam is a direct indicator of the intensity and beam profile of the fundamental laser beam. A computer program runs the learning algorithm with photodiode signal as input and deformable mirror shape as its output. A deformable mirror shape is chosen, and the learning algorithm monitors the photodiode signal over several laser shots. Several slightly different deformable mirror shapes are then chosen and the photodiode signals are monitored again. The mirror shape that gave the highest photodiode signal is chosen and then modified slightly to provide several more mirror profiles. This process of improvement-evolution is continued until the photodiode signal does not improve from one mirror shape to the next.

Target manipulation stage

To make full use of the extremely tight focus produced by the deformable mirror system, the target of interest must be moved in a way that reduces its perturbations

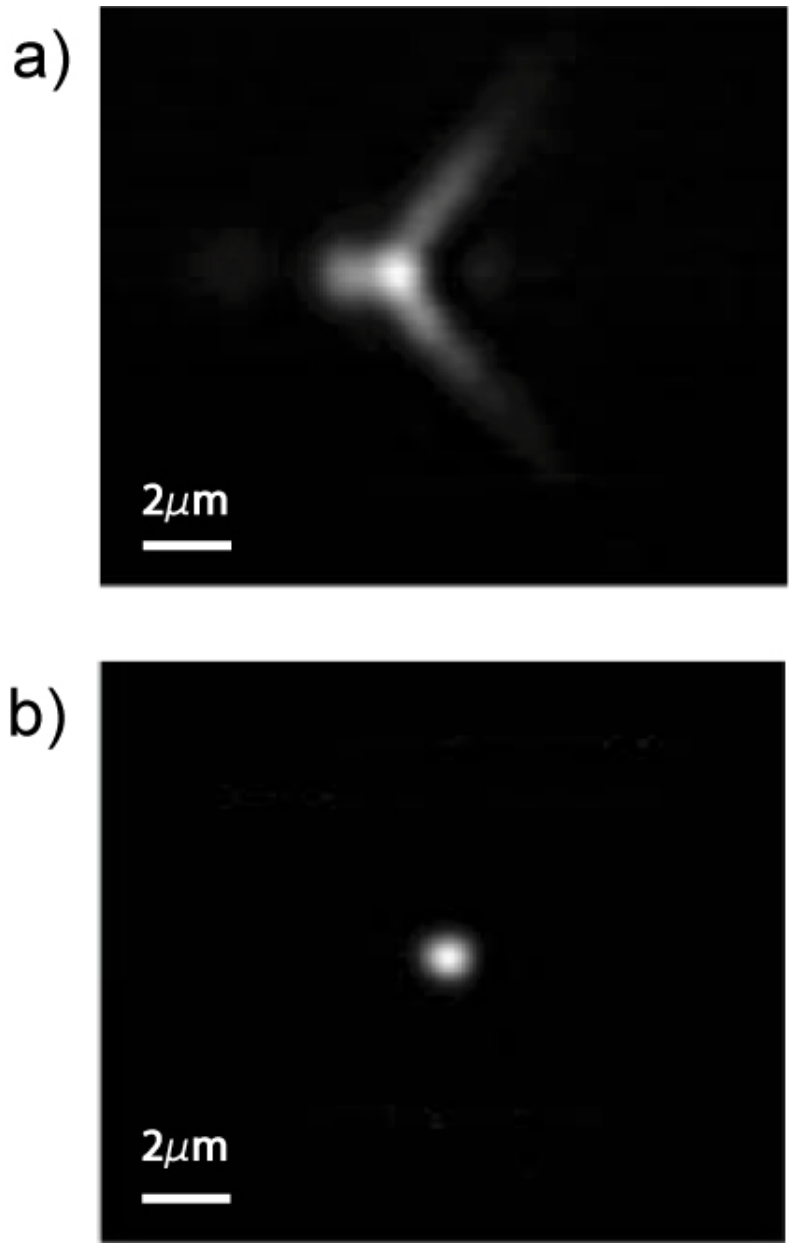

Figure 2.2: (a) An image of the pump beam focal region made with the deformable mirror set as a flat. The $f/1$ paraboloid is set to best focus. Aberrations are cumulative for all optics in the system, including imperfections in the paraboloid. (b) Pump beam focal region after correction by the computer learning algorithm and deformable mirror. The tightest beam produced has a diameter of 1.2 μm FWHM.

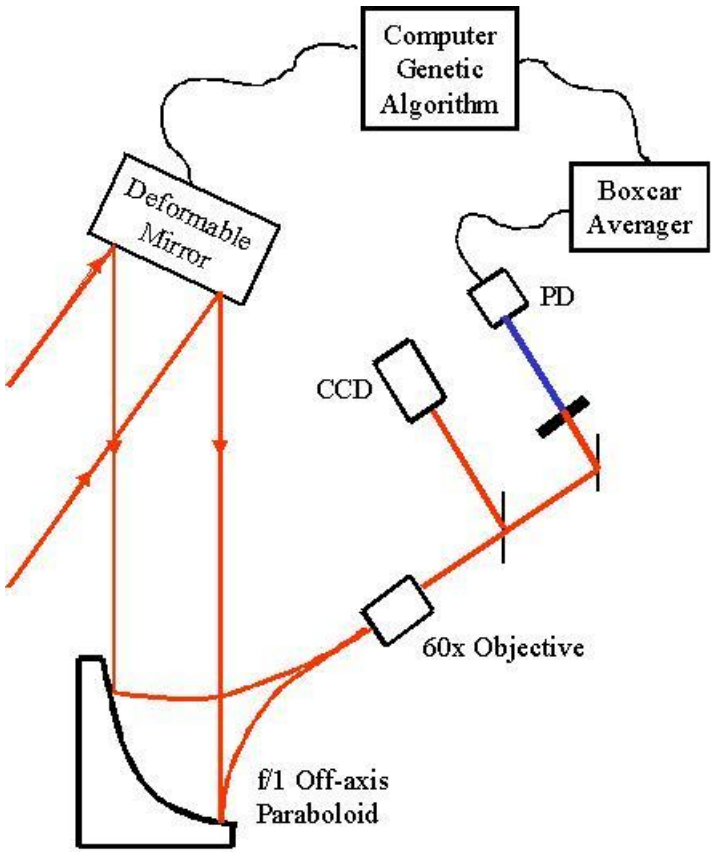

Figure 2.3: This is the deformable mirror imaging setup.

to distances that are approximately the wavelength of the laser beam. Stable target motion is accomplished by using a precision bearing stage as the main rotating element of the the target manipulator. Carefully ground bearings in this rotating element, combined with main components machined from a low-thermal-expansion metal alloy, reduce the rotational wobble of the target manipulator to less than 2 μm. This rotation stage is belt driven by a precision servo motor. Lateral translation of the target is handled by a commercial translation stage and precision servo motor. Each servo motor includes a position encoder so that the computer control system may monitor and record the position of the stage to less than 0.1 μm accuracy. In most experiments using this system, lateral slop is much less of a concern than movement in the $\hat{z}$ direction (along the direction of laser propagation). Target motion in the $\hat{z}$ direction is controlled by a third encoding servo motor and precision translation stage. In typical experimental runs, the $z-$position of the target with respect to the focal volume of the pump laser pulse is set and not changed during the course of an experimental run. In practice this entire system performs very well. This entire target manipulation stage is placed inside a vacuum chamber. Typical experiments are performed with the chamber evacuated to 10^{-3} torr level.

Both $S-$ and $P-$polarized pump beams were used in these experiments. Rotation of the pump beam polarization was done by passing the beam through a high quality, 85 μm thick mica $\lambda/2$-plate. The small thickness of this wave plate helps keep optical abberations and accumulated B-integral [30, 31] to a minimum. B-integral is of particular concern because the polarization rotation is done on the compressed laser pulse, rather than the uncompressed pulse, due to design requirements of the optical compressor.

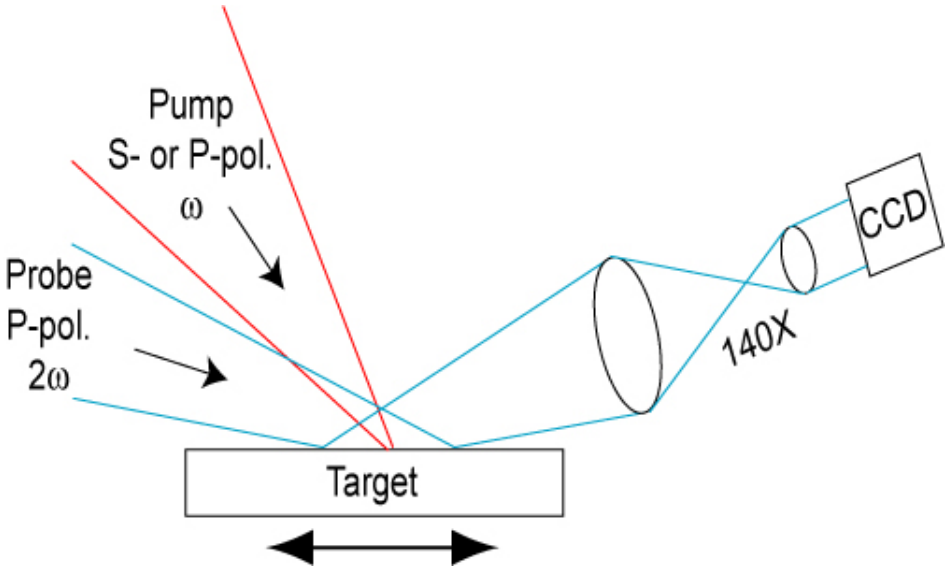

Figure 2.4: Diagram of the pump-probe experimental setup.

Probe beam imaging system

In all of the experiments presented in this work, the plasma created at the focus of the intense laser pulse is observed by a low-intensity, time delayed, second harmonic laser pulse. This probe laser pulse is created by splitting off a fraction of the main laser pulse and frequency doubling it to $\lambda_{probe} = 400$ nm in a 0.48 mm thick KDP crystal. [32, 33] The amount of 800 nm light split off to form the probe beam is a bit higher than typical for high intensity experiments, but here it is important to remember that the high intensity comes from tight focusing, not from tremendous pump beam energy. In order to form a second harmonic beam that is bright enough to be observed at the end of the probe-imaging optics chain, including a loose focus and reflection off of the experimental target, a fairly bright input beam must be used. In present configuration approximately 15% of the pump beam is split off to form the probe beam. Such a large fraction of total pump energy is necessary to

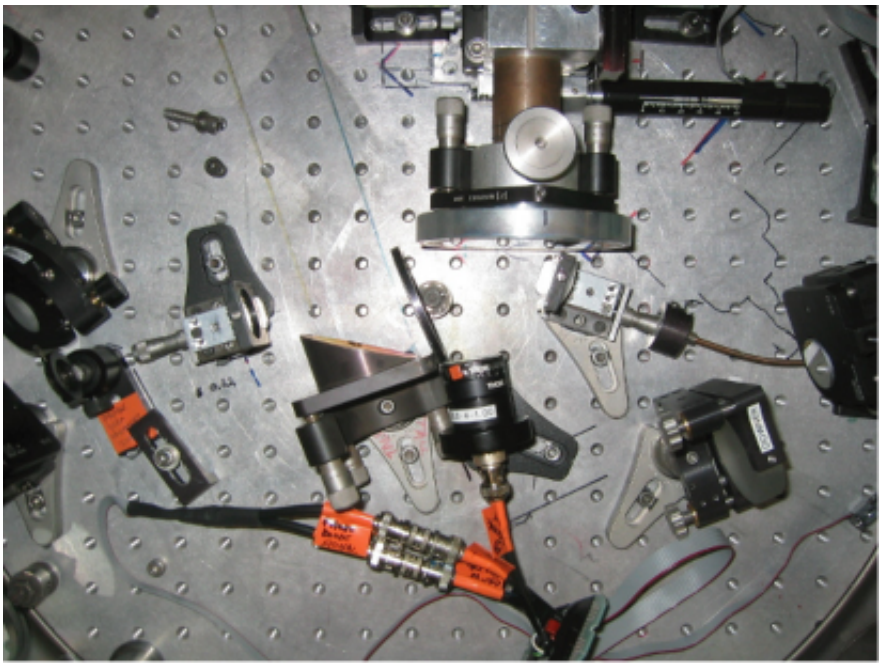

Figure 2.5: Photograph of the experimental setup inside the target vacuum chamber. The paths of the 800 nm pump and 400 nm probe beam are designated. The probe beam enters the chamber from the left side of the photo. The precision target manipulator stage is partially shown near the top of the photograph. The probe beam exits the chamber to the right of the photograph and goes to the 10× microscope objective.

counter the losses on several aluminum mirrors ($R \approx 0.9$ each) and conversion losses in the KDP crystal. This probe pulse is time-delayed with respect to the main pulse. Any residual 800 nm light after the KDP crystal is removed by passing the beam through a 1 mm thick piece of Schott BG39 glass.

To obtain high resolution images of the probe beam, a large aperture primary optic was used close to the target. This $f/2$ lens has a clear aperture of 25 mm and is an achromat made of graded-index glass (Newport GAC060 a.k.a. LightPath Gradium). While we do not make use of the improved color focusing of the achromat (the probe beam bandwidth is only $\sim$ 15 nm FWHM), this type of lens provides

the advantage of being corrected for spherical abberations. Also, the graded index glass gives improved focusing quality over typical uniform index glass. Although most microscope objectives have greater numerical aperture, this $f/2$ achromat is the highest numerical aperture optic available that can physically fit into the experimental setup. Constraints on the size of this optic are the distance of the optic to the pump beam focal spot on the target and the angle of reflection of the probe beam off of the target. Magnification of the micron-scale plasma region is provided by placing the image formed by the achromat at the object plane of a $10\times$ microscope objective a distance of 70 cm ($14f$) away. A microscope objective was chosen because it has a high numerical aperture (NA = 0.25) and is well corrected for a number of abberations. We have chosen to use an air-spaced objective due to cost constraints. A non-interlaced, low noise, monochrome CCD camera is placed in the image plane of the microscope objective. Both the achromat and microscope objective are placed on translation stages so that focusing may be optimized. A mechanical vacuum feed through is coupled to the achromat translation stage so that it may be adjusted while the target chamber is under vacuum. Additionally, the microscope objective is mounted in a tip-tilt mirror mount so that its axis may be aligned with the probe beam propagation $\vec{k_z}(x, y)$. With this setup, an overall magnification of $140\times$ is achieved and we are able to obtain highly detailed images with resolution of better than 0.5 μm.

Data acquisition

Most systems in this experiment are controlled by a single computer with LabVIEW software. This greatly improves the quality of the data because the movement of the target, the movement of the probe delay stage, opening of the laser shutter and

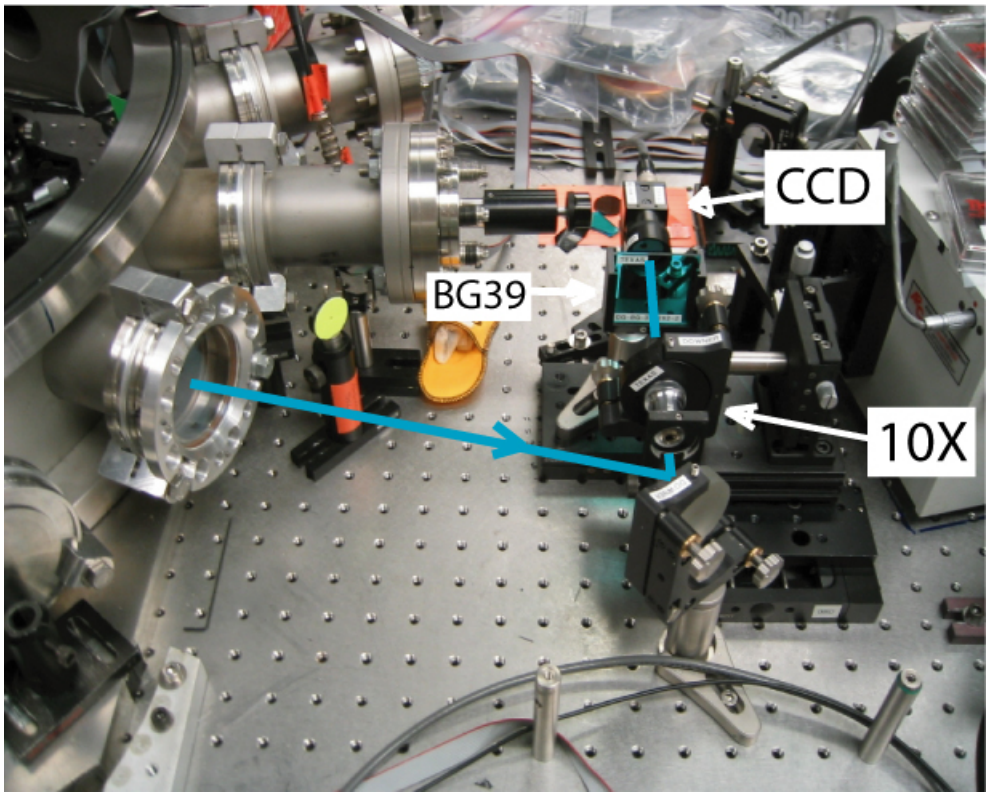

Figure 2.6: Photograph of the final stage of the probe beam imaging system. Each component is mounted on a tip-tilt and $x-y$ translation stage to allow for precision optimization of the imaging. This system delivers resolution better than 0.5 μm at $\lambda_{probe} = 400$ nm.

recording of CCD images all begin, end, and are completely monitored simultaneously by computer. The target is rotated and translated quickly enough so that each laser pulse is incident on fresh target material. As the probe beam delay stage is moved, the position of the stage is recorded and added to the filename of the image taken at that probe delay. Each CCD image is recorded in real time to the computer hard disk as a bitmap file. These features make analyzing the probe images and determining the time evolution of the plasma much easier.

Targets

The tight focusing of the pump beam causes the pump beam to have a very short range of focus (the Rayleigh range). The Rayleigh range is defined as [34, 35]

$$z_R = \frac{\pi w_0^2}{2\lambda} \tag{2.1}$$

For a pump beam wavelength $\lambda = 800$ nm and beam waist $w_0 = 0.75$ μm (1.5 μm diameter), the Rayleigh range $z_R = 2.2$ μm. Consequently, targets that are very flat across the entire surface are required. For these experiments, we use aluminum and copper targets that are 100 mm diameter, 13 mm thick and have $\lambda/2_{632nm}$ flatness across the entire surface. These targets were purchased from Kugler of America, a high precision custom optics house. We also purchased one polypropylene target cut to the same specifications, but the plastic nature of polypropylene made the target surface too lumpy and distorted to use.

Chapter 3

Chapter 3 – Theory

3.1 Diffusive energy transport

If the characteristic length of energy transport is smaller than the region of interest, the movement of heat in a material may be modeled as diffusive transport. In this process, energy emitted by the material travels a short distance before being reabsorbed by the material. The heat flow $\vec{Q}$ is described by the equation

$$\vec{Q} = -\kappa(T_e)\nabla T_e, \tag{3.1}$$

where $\kappa(T_e)$ is the temperature-dependent diffusivity. [36, 37, 38, 39, 40, 41] This equation is general and may be applied to a variety of situations, from the cooling of coffee in a pot to the cooling of a hot plasma, by inserting the appropriate diffusivity.

As has been shown by Spitzer [38, 39], energy transport in a plasma is dominated by Coulomb collisions of plasma electrons for plasma temperatures of less

than 100 eV. [42] In this case the thermal electron diffusivity is

$$\kappa_{SH} = \frac{4T_e^{5/2}}{Ze^4 m_e^{1/2} \ln \Lambda} \tag{3.2}$$

where Z is the ionization state of the material, e the electron charge, m_e the electron mass and $\ln \Lambda$ is the Coulomb logarithm. [43, 37, 41] This diffusivity is non-linear in temperature, going as $T_e^{5/2}$. In this process the mean free path for electron-ion collisions

$$\lambda_{ei} \approx (10^{17}) \frac{[k_B T_e]^2}{Z^2 n_i} [\mu\text{m}] \tag{3.3}$$

This relation defines the scale sizes of interest for thermal diffusion in a plasma of some temperature. If λ_{ei} is shorter than the scale length or density gradient of the plasma, then diffusive thermal transport may be applied. However, if λ_{ei} becomes about the same size as or larger than the plasma scale size a different transport theory must be used to describe the system.

For plasma electron temperatures greater than about 100 eV, radiative transport dominates over the collisional-electron transport. In this case, the diffusivity κ becomes

$$\kappa_{rad} = \frac{16}{3} \sigma_{SB} T_e^3 \lambda_{Rosseland} \tag{3.4}$$

where $\lambda_{Rosseland}$ is the radiative mean free path and σ_{SB} is the Stefan-Boltzmann constant. [36, 42, 44]

$$\lambda_{Rosseland} = 9 \times 10^6 \frac{T_e^2}{Z^2 n_i} e^{I/k_B T_e} [\text{cm}] \tag{3.5}$$

Notice that the total radiative diffusivity κ_{rad} is proportional to T_e^5, making the process of radiative diffusion highly non-linear. A small increase in plasma electron

temperature will yield a tremendous gain in energy transport through the material. Implicit in these equations is the assumption that the plasma may be considered an ideal gas and in local thermodynamic equilibrium (LTE). For low density plasmas, this assumption is valid but it begins to become questionable as the plasma density becomes "over-dense" or "solid-density".

The radiative and electron-ion mean free paths, $\lambda_{Rosseland}$ and λ_{ei}, determine the size and temperature parameters over which the diffusive transport theory is valid. If the mean free path λ_{mfp} is much smaller than the size of the plasma region being studied, then diffusive transport should describe observations quite well. [45] However, as the mean free path becomes approximately the same size as or larger than the size of the plasma, the diffusive theory breaks down and becomes less appropriate. [46, 47] In this regime energy transport becomes non-local and other transport theories must be used, such as kinetic models or particle-in-cell simulations that directly account for the effects of radiation emission and absorption in the plasma.

Resonance Absorption

One of the main absorption processes of a laser by a plasma is resonance absorption. [48, 49] The experiments presented in this work depend on resonance absorption of a probe laser pulse to observe the expanding, heated plasma. [50] In the resonance absorption process a $P-$polarized laser pulse is obliquely incident on a plasma region with an electron density gradient. The electric field of the laser light has a vector component that lies parallel to the plasma density gradient. As the light penetrates deeper into the plasma gradient, the frequency of the light ω approaches the plasma

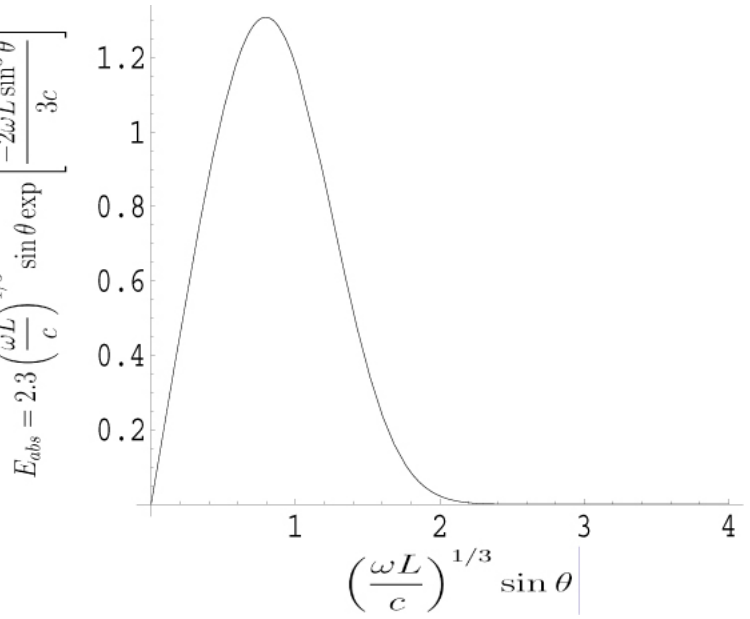

Figure 3.1: Analytic calculation of 1-D resonance absorption using equation 3.12.

frequency ω_e:

$$\omega_e = \left(\frac{4\pi e^2 n_e}{m_e}\right)^{1/2} \tag{3.6}$$

The oscillations of the light cause the electrons in the plasma to oscillate along the direction of the density gradient. This causes the energy carried in the light to be transferred to the plasma electrons, further exciting and heating the plasma. For $S-$polarized light, the electrons are excited to motions parallel to the plane of the plasma. This excitation couples no energy into the plasma and results in almost complete reflection of the light.

Critical density is the density of electrons in the plasma at which the plasma frequency is equal to the frequency of the incident electromagnetic radiation (laser

light). From Kruer's book [43] (p. 12):

$$\omega_{Pe} = \sqrt{\frac{4\pi n_e e^2}{m_e}} \tag{3.7}$$

where n_e is the electron density, e is the electron charge, m_e is the mass of the electron and the subscript Pe on ω_{Pe} signifies that this is the oscillation frequency of the *electrons* in the plasma (as opposed to the ion oscillation frequency). If the electron density n_e is expressed in units of cm^{-3}, then:

$$\omega_{Pe} = 5.64 \times 10^4 \sqrt{n_e}\ [\mathrm{s}^{-1}]. \tag{3.8}$$

The density n_e at which the plasma frequency ω_{pe} is equal to the incident light frequency, ω_e, is called the critical density, n_{crit}. For the probe laser wavelength of 400 nm used in the experiment, the critical density is

$$\omega_{pe} = \frac{c}{2\pi\lambda} = 5.64 \times 10^4 \sqrt{n_{crit}}, \tag{3.9}$$

Thus:

$$n_{crit} = \left[\frac{1}{5.64 \times 10^4}\frac{c}{2\pi\lambda}\right]^2 = \left[\frac{1}{5.64 \times 10^4}\frac{3 \times 10^{10}\ \mathrm{cm/s}}{2\pi(0.4 \times 10^{-4}\ \mathrm{cm})}\right]^2. \tag{3.10}$$

$$n_{crit}^{400\ \mathrm{nm}} = 4.48 \times 10^{18}\ \mathrm{cm}^{-3} \tag{3.11}$$

For comparison, the solid density of aluminum (at 293K) is 6.02×10^{22} cm^{-3}. [51] Following the standard description of resonance absorption [43, 6], for a 1-D linearly

expanding plasma the absorbed electric field is:

$$E_{abs} \propto 2.3 \left(\frac{\omega L}{c}\right)^{1/3} \sin\theta \exp\left[\frac{-2\omega L \sin^3\theta}{3c}\right]. \tag{3.12}$$

A plot of this equation appears as figure 3.1. As the plasma expands outward, the light penetrates deeper into the plasma up to the critical surface where it is absorbed. As the plasma continues to expand, the light is reflected by the sub-critical density plasma before it reaches the critical surface. This is shown in the figure as $(\omega L/c)^{1/3} \sin\theta$ increases to values > 1.

3.1.1 Opacity

The opacity of a material is a measure of the absorption process that removes photons from a beam of light passing through the material. [40, 36, 52] As the beam of light propagates, some of the light energy is lost to the material through a variety of processes, such as scattering and absorption. Opacity, $\chi(\vec{x}, t, \vec{n}, \nu)$, is the sum of all of these processes (for specified radiation frequency, position, and plasma density), and has dimension of $[length^{-1}]$. The inverse of opacity is sometimes called the photon mean free path or the optical depth in the material. A material's opacity is dependent on a number of properties of the material. In particular, it depends strongly on the material density and temperature. Opacity also depends on the frequency of the light propagating in the material.

Knowledge of the opacity of a material is very important when considering radiative transport in the material. Material opacity will determine how far the radiation will travel before its energy is absorbed by the material. Opacity will also determine which energy transport processes are dominant. [53, 54, 25, 24]

3.2 Surface Electron Transport and Heat Wave Propagation Speed

As the temperature of the plasma begins to exceed about 1 keV, energy transport via ballistic hot electrons becomes important. [55, 56, 57, 58, 59, 60] For our experiments this process is significant because the size of the initially heated plasma is so small compared to the travel distance of these electrons. [61] We will discuss later that this process dominates over radiative transport in our experiments. The motion of these fast electrons forms an electrical current and causes a magnetic field to develop. The electron motion then becomes confined and guided by this self-generated $B-$field. [62, 63] This causes the energy deposited by the laser pulse to be spread preferentially in a plane.

In order to understand the motion and confinement of the hot electrons produced during the laser-plasma interaction we first want to evaluate the angular component of the self-generated magnetic field B_θ. [64] Beginning with Maxwell's equations:

$$\frac{\partial B_\theta}{\partial t} = -\left(\nabla \times \vec{E}\right)_\theta . \tag{3.13}$$

We can write down the equation of motion for an electron in an external electric field (*i.e.* the laser field): [65]

$$m\frac{d\vec{v}}{dt} = -e\vec{E} - \frac{1}{n_e}\nabla P_e = 0, \tag{3.14}$$

where $P_e = n_e T_e$ is the electron pressure, n_e is the electron density and T_e is the electron temperature in [eV]. If the electric field is quasi-static we may ignore the inertia of the electrons. This is because the electron does not change directions of motion quickly since the driving electric field is oscillating slowly. Any effects from

quickly changing the acceleration direction of the electrons is approximately zero. Now, in general, we may rewrite Maxwell's equation using the information from equation [65, 64] (3.14).

$$\nabla \times \vec{E} = -\nabla \times \left[\frac{1}{en_e} \nabla (n_e T_e) \right] \tag{3.15}$$

$$= \frac{1}{en_e} \nabla n_e \times \nabla T_e, \tag{3.16}$$

Working out the derivatives the angular component of the magnetic field B_θ is

$$B_\theta = -\int_0^{t'} dt \frac{1}{en_e} \frac{\partial n_e}{\partial z} \frac{\partial T_e}{\partial r} \tag{3.17}$$

$$= -\frac{1}{e} \frac{1}{\lambda_D} \int_0^t dt \left(\frac{\partial T_e}{\partial r} \right) \tag{3.18}$$

$$B_\theta \approx -\frac{1}{e} \frac{1}{\lambda_D} \frac{T_e}{L_T} \tau \tag{3.19}$$

where $L_T(t)$ is the transverse temperature profile of the plasma (ie: plasma scale length), λ_D is the electron Debye length, and τ is the timescale of interest. The Debye length in a plasma is [41, 66, 43]:

$$\lambda_D = \sqrt{\frac{\epsilon_0 T_e}{n_0 e^2}} \text{ for } T_e \text{ in [eV]} \tag{3.20}$$

The electric field E_z of the plasma sheath is:

$$E_z = -\frac{\partial \phi}{\partial z} \approx \frac{T}{e} \frac{1}{\lambda_D} \tag{3.21}$$

We must compute the Debye length for plasma parameters of the experiment to make sure that it is smaller than the scale length of our experiment. For an electron density $n_0 \sim 10^{21}$ cm^{-3} (approximately solid density) and electron temperature

$T_e \sim 10$ keV, the Debye length is $\lambda_D \approx 2 \times 10^{-6}$ cm. This is about $1/100^{th}$ the size of our initially heated plasma region. Next, we should determine the heat front propagation velocity v_r as it moves out of the heated region [41]:

$$v_r = \left(\frac{\vec{E}_z \times \vec{B}_\theta}{B_0^2} \right)_r \tag{3.22}$$

$$= -\frac{E_z}{B_\theta} \tag{3.23}$$

$$v_r = \frac{-\left(\frac{T_e}{e\lambda_D}\right)}{-\frac{1}{e}\frac{1}{\lambda_D}\frac{T_e}{L_T}\tau}. \tag{3.24}$$

This reduces to:

$$v_r = \frac{L_T}{\tau}. \tag{3.25}$$

For our experiment where we have an initially micrometer scale plasma ($L_T \sim 10^{-4}$ cm) and observing over a picosecond ($\tau \sim 10^{-12}$ sec), the heat front propagation velocity $v_r \approx 10^8$ cm/sec. This matches well with the data that will be presented later in this manuscript.

The motion of the hot electrons produced in our experimental plasmas is very important. In order to further understand the physics behind this process it is helpful to notice that equation (3.22) is the same as the electric field drift of the plasma guiding center. Here we provide the basic outline of this concept. For a more detailed approach, the book by Chen [67] does a nice job of deriving this result in general. Here we shall start with the equation of motion of an electron in external electric and magnetic fields:

$$m_e \frac{d\vec{v}}{dt} = q\left(\vec{E} + \vec{v} \times \vec{B}\right). \tag{3.26}$$

To get a general formula for the drift velocity of the guiding center $\vec{v}_{gc}$, we must

solve the equation of motion for $m_e \frac{d\vec{v}}{dt} = 0$ because the force term refers only to the circular motion of an electron at the plasma cyclotron frequency. [41] Consequently:

$$\vec{E} + \vec{v} \times \vec{B} = 0. \tag{3.27}$$

Rearrange and take the cross product of both sides with $\vec{B}$ and we obtain:

$$\begin{aligned} \vec{E} \times \vec{B} &= \vec{B} \times \left(\vec{v} \times \vec{B} \right) && (3.28) \\ &= \vec{v}B^2 - \vec{B} \left(\vec{v} \cdot \vec{B} \right) && (3.29) \end{aligned}$$

The transverse components of equation (3.29) are:

$$\vec{v}_{gc,\perp} \equiv \vec{v}_E = \frac{\vec{E} \times \vec{B}}{B^2} \tag{3.30}$$

Thus, $\vec{v}_E$ is the electric field drift velocity of the guiding center. The magnitude of this velocity is:

$$v_E \text{ [m/s]} = \frac{E \text{ [V/m]}}{B \text{ [tesla]}} \tag{3.31}$$

Consequently, one may estimate the magnetic field strength from the observed drift speed of electrons.

Chapter 4

Chapter 4 – Experimental Data

4.1 Energy transport dominated by radiation

The first series of data we obtained from this experiment was done with an early incarnation of the λ^3 Laser. The pump pulses used had duration $\tau = 24$ fs, energy of approximately 1 mJ and pulse temporal contrast ratio of $1 : 10^{-5}$. The probe beam was incident on the target at $\theta_{pr} = 60^{\circ}$ with a spot size of about 10 μm centered on the pump spot.

The data shows radial expansion of a central dark region initially excited by the intense pump laser pulse on an aluminum target. Several selected images are shown in figure 4.1 We observe the expansion of this region over the course of 1 ps via the time delayed probe beam. When using an $S-$polarized probe beam, we do not observe any change in the reflected brightness. For a $P-$polarized probe beam, the brightness of the beam reflected from the target drops quickly. This change in reflectivity matches the change predicted by 1-D resonance absorption theory. We have plotted the probe reflectivity versus probe beam time delay for aluminum targets excited at 1.8×10^{18} W/cm^2 in figure 4.4. Fitting the 1-D resonance absorption

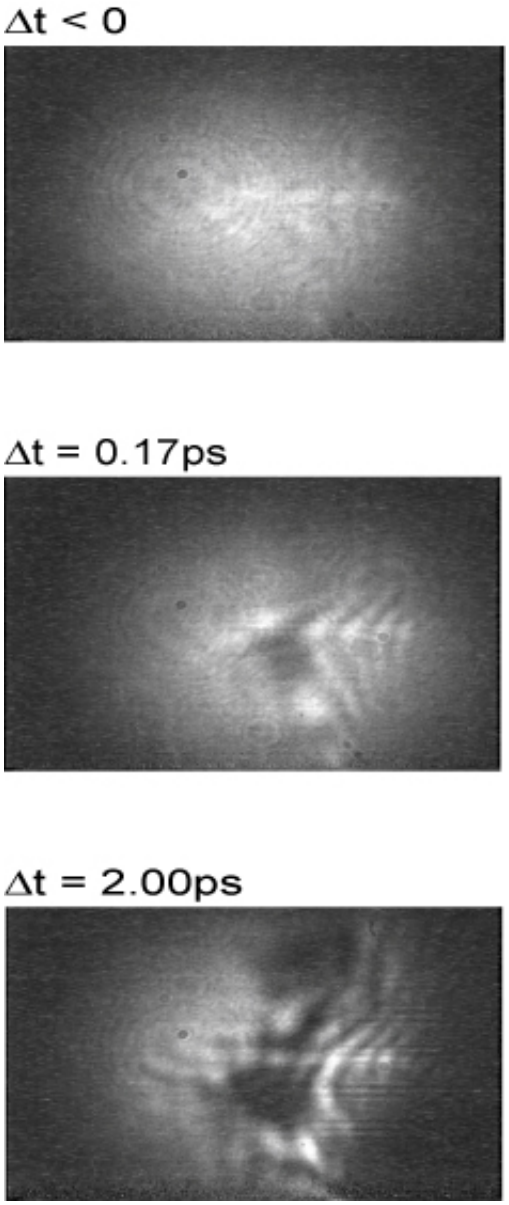

Figure 4.1: Images of a radially expanding aluminum plasma observed via resonance absorption of a $\lambda_{probe} = 400$ nm probe laser pulse at different pump-probe time delays. This plasma was excited by 25 fs, ≈ 1 mJ, $\lambda_{pump} = 800$ nm laser pulses focus to intensity $I_{pump} = 1 \times 10^{18}$ W/cm^2. The plasma region expands out from the initially pump-excited ($\omega_0 \sim 1.5$ μm) region at $v_{radial} \approx 10^8$ cm/s.

theory to the curve indicates that the plasma produced on the target expands vertically into vacuum at $v_z = 2 \times 10^7$ cm/s. For all measurements on these data, probe time delay = 0.0 ps is set to be the point where the probe beam reflectivity begins to drop. The probe beam reaches maximum absorption 0.25 ps after excitation by the intense pump pulse.

With images taken with the $P-$polarized probe beam, we plot lineouts from the images showing the radial expansion of the plasma region. Data taken at pump intensity of 3.7×10^{17} W/cm^2 shows very brief expansion of the plasma region beyond the size of the initially excited pump laser focus (recall that the pump laser focus is ≈ 1 μm). However, at the highest pump laser intensity of 1.8×10^{18} W/cm^2 the plasma region expands radially to much larger than the initially excited region within 1 ps of pump excitation. These data are shown in figure 4.2. The overall size of the radially expanded plasma region is comparable to the size of x-ray source spots taken in separate measurements. [68] Additionally, diffraction features appear in the images at later time delays. This is due to the vertically expanding plasma becoming more spherical and scattering the probe beam light away from the collection cone of the imaging optics.

We have successfully modeled the radial expansion of the heated plasma region by applying radiative diffusion theory. [69] The details of this analysis are described elsewhere in this document. This analysis describes the overall radial expansion size of the heated plasma region quite well, but it does not adequately match the early time dynamics of the system as shown in figure 4.3. Due to the incredibly small focal spot size of the intense pump pulse and, consequently, the small size of the initially heated plasma, it is likely that energy transport over times $\tau < 0.5$ ps is dominated by non-local radiative transport and/or ballistic hot

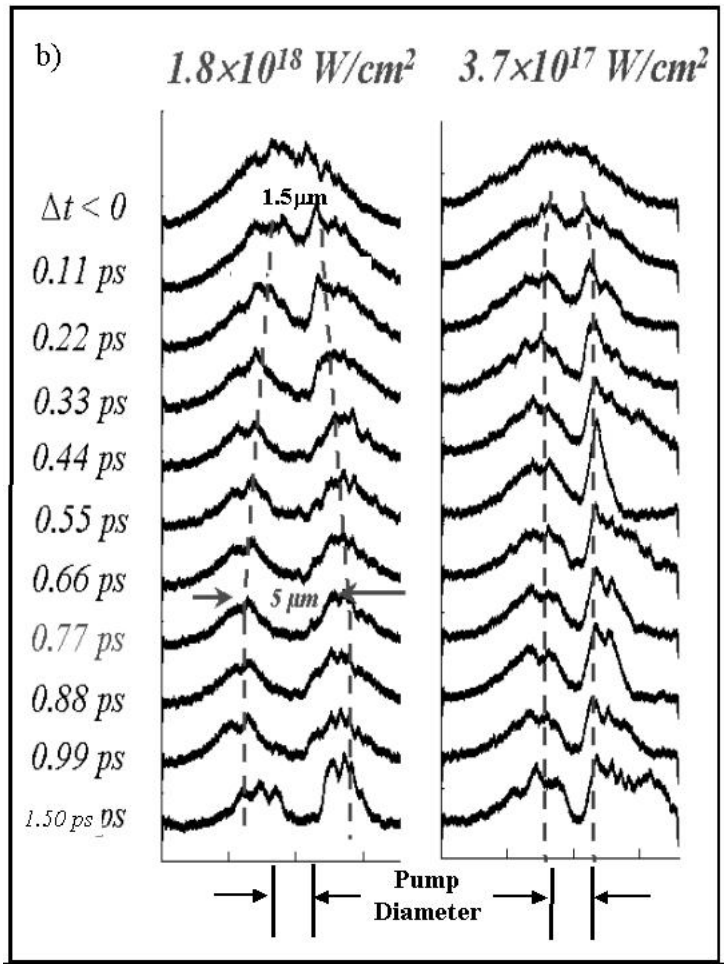

Figure 4.2: Lineouts from probe images at two different pump laser intensities. Background noise was subtracted from each image. The radial expansion of the laser-excited region is evident at the highest pump intensity (left) but nearly absent at the fivefold lower pump intensity (right).

electrons.

4.1.1 Data Processing

Through the course of the experiment, we record up to several thousand images per data run. With such a huge quantity of information there needs to be several computer automated ways of processing the data. All of the image processing is done using ImageJ [70], a product of the National Institutes of Health. ImageJ has a number of built-in image processing functions. It also allows background noise to be removed from each image by subtracting a null image from each image in the data set.

To measure the reflectivity of the probe beam from the plasma, an ImageJ routine was written to sum the pixel intensity values of a chosen region. The same region was selected from each image, summed, and the results were written to a file. By normalizing these values, the relative changes in probe beam reflectivity may be plotted versus probe beam time delay. This was done for both $S-$ and $P-$polarized probe beams. Typical results are shown in figure 4.4. It is clear that the probe beam is being absorbed by the plasma through resonance absorption. The drop in reflectivity of the $P-$polarized probe beam matches quite well the characteristic reflectivity change for 1-D resonance absorption (RA). We have calculated the 1-D resonance absorption curve for our plasma parameters, and that result is plotted in figure 4.4 as well. We assume a constant vertical plasma expansion velocity of $v_z = 2 \times 10^7$ cm/s for the RA calculation.

Lineouts from each image are taken so that the size of the expanding plasma region may be measured. Again, these lineouts were produced using ImageJ subroutines. The lineouts were written to a file and then post-analyzed using MATLAB

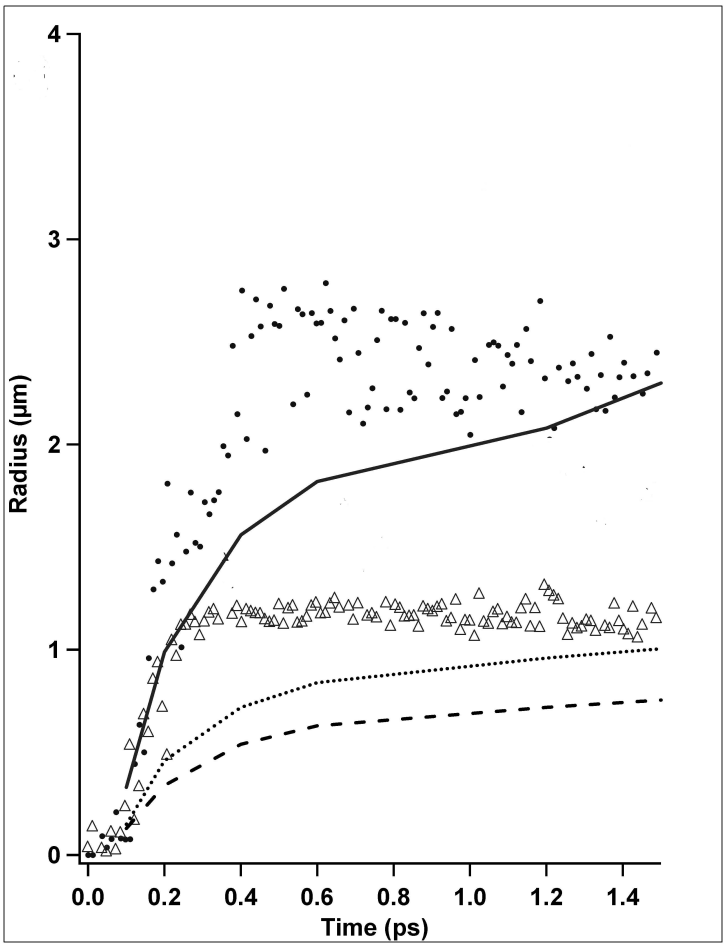

Figure 4.3: Radius of the laterally expanding plasma region, as observed by resonance absorption of the probe beam, plotted versus pump-probe time delay. Data taken at pump intensity of 1×10^{18} W/cm^2 is shown as solid black squares. Data taken at pump intensity of 3.7×10^{17} W/cm^2 are plotted as open triangles. Plasma heating and expansion due to diffusion of both radiation and coulomb collisions for 0.88 mJ absorbed on target ($\sim 10^{18}$ W/cm^2) is plotted by the solid black line. Note that this calculation matches well the overall size of the heated region but does not recreate the details of the early-time dynamics. The dashed line shows minimal plasma expansion when radiative transport is turned off in the computations. We also calculate the expansion for 0.20 mJ absorbed on target ($\sim 3 \times 10^{17}$ W/cm^2) including both radiation and collisional transport. These results are shown by the dotted line.

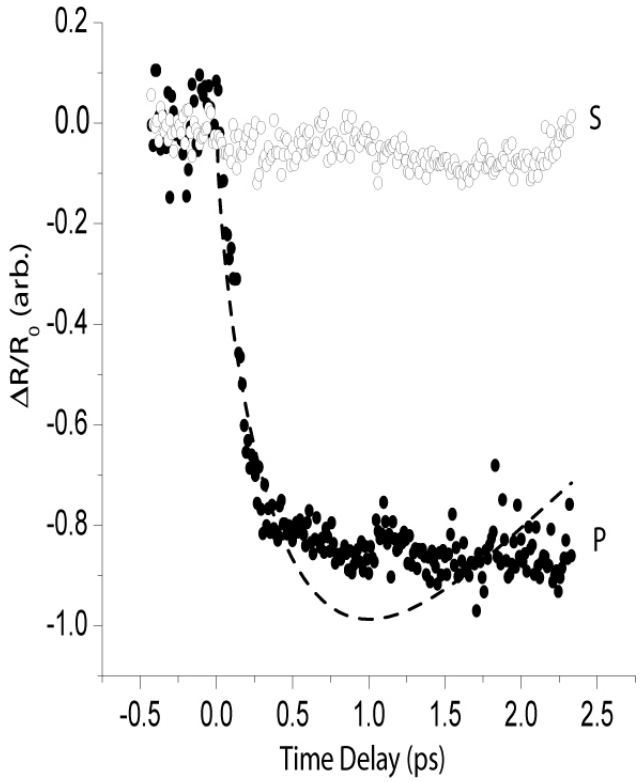

Figure 4.4: Normalized S- and P-polarized probe beam reflectivity $\Delta R^{S,P}_{probe}/R_0$ at the center of the pump-excited spot for $I_{pu} = 1.8\times10^{18}$ W/cm^2. Dashed curve: fit of $\Delta R^{P}_{probe}(\Delta t \leq 0.5$ ps) data to a 1-D resonance absorption (RA) model [W. L. Kruer, *The Physics of Laser Plasma Interactions*] assuming constant vertical expansion velocity $v_z = 2 \times 10^7$ cm/s. At longer Δt, 3-D effects and time dependence of kT_e complicate RA.

software. First, the pixel intensity values were background subtracted and normalized. The width of the expanding plasma region was measured between points at the half-height of the absorption dip in the lineouts. The pixel widths were then converted to micrometer lengths by backing out the magnification of the imaging system convolved with the physical pixel dimension of the CCD camera.

In these experiments, both aluminum and copper targets were used in order to explore the effects of increasing Z on the dynamics of the plasma expansion. By varying the pump beam polarization the effect of different pump beam absorption by the target is explored. Data was taken for two laser intensities; 1×10^{18} W/cm^2 and 1×10^{17} W/cm^2.

Table 4.1: Table showing the fraction of pump laser light absorbed by different target materials for both $P-$ and $S-$polarization at 10^{18} W/cm^2 and 10^{17} W/cm^2 for the second set of experimental data. These absorptions were measured with a filtered photodiode placed inside the target vacuum chamber.

Material	**Intensity [W/cm^2]**	**Pump Polarization**	**Fraction Absorbed**
aluminum	10^{18}	P	80.8%
aluminum	10^{18}	S	77.8%
aluminum	10^{17}	P	57.1%
aluminum	10^{17}	S	42.4%
copper	10^{18}	P	80.0%
copper	10^{18}	S	68.0%
copper	10^{17}	P	56.2%
copper	10^{17}	S	36.5%

Pump pulse absorption data was obtained by placing a photodiode inside the target vacuum chamber at various locations. See figure 4.5 for a diagram. Several layers of neutral density filters and an 800 nm interference filter were used to attenuate the light and keep the response of the photodiode linear. Reference intensity

measurements were taken by placing the photodiode in the path of the incident pump pulse. The energy of the pump pulse is known from separate measurements with a laser power meter. The photodiode signal can be calibrated to this energy measurement by backing out the effects of the neutral density and interference filters, and accounting for the small active area of the photodiode as compared to the diameter of the incident laser beam. These measurements were taken at both 10^{18} W/cm^2 and 10^{17} W/cm^2. The face of the photodiode was positioned to be normal the the incident beam, so for this calibration measurement there is no difference between $P-$ and $S-$polarizations. These measurements were averaged over several thousand laser pulses. Measurements of the amount of light reflected from the target (and emitted from the plasma produced) for different pump laser polarizations were obtained. Because of the long time response of the photodiode compared with the temporal duration of interest of the experiment, these measurements are time integrated. The photodiode was placed in two different locations for these measurements: (1) in the specularly reflected beam path with its face normal to the propagation direction; and (2) outside of the specular reflection with the face of the photodiode oriented normally to a line connecting the photodiode to the target plasma region. The photodiode measurements were averaged over several thousand laser shots. Effects due to the area of the photodiode were accounted for by comparing with the surface area of a half-sphere of radius equal to the distance of the photodiode from the target.

4.1.2 Modeling diffusive energy transport within the plasma

In order to understand the nature of the rapid radial expansion of the plasma we observe in the experiments, we have computationally modeled the diffusion of radia-

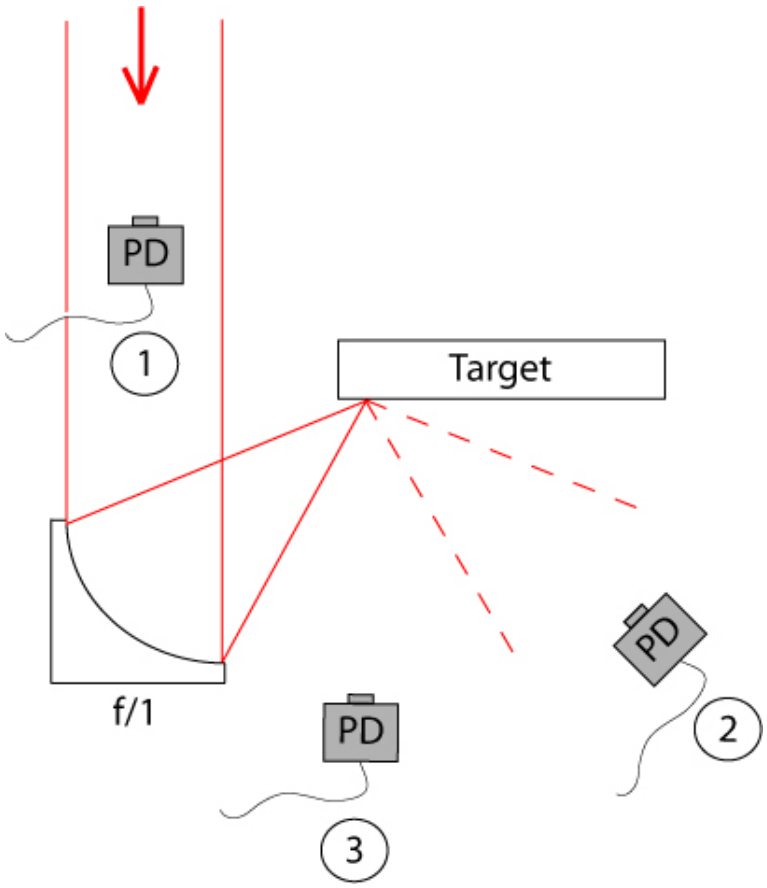

Figure 4.5: Placement of the photodiode for measurements of amount of pump beam energy absorbed by the target material. Position (1) is the input beam, position (2) is in the path of pump beam specular reflection, and position (3) is outside the specular reflection path.

tion and collisional electrons within a micrometer sized plasma. [71, 72] Using these computer models we perform the computational analysis of the data in four main steps: (1) evaluation of the plasma temperature profile $T_e(r, z, t)$ under excitation by the intense pump pulse; (2) calculation of the expanding plasma density $n_e(r, z, t)$; (3) determination of the location of the plasma critical surface $z_{crit}(r, n_e, t)$ where resonance absorption of the 400 nm probe pulse takes place; (4) calculation of the imaging of the probe beam accounting for the expanding plasma surface and the finite aperture of the imaging optics. [73]

Plasma Temperature Profile Calculation

To determine the plasma temperature profile $T_e(r, z, t)$, we first represent the intense pump laser pulse by a Gaussian profile with width of 0.75 μm, 25 fs length and constant fluence E_L. It is assumed that the laser pulse is completely absorbed by the aluminum to a depth of 300 nm. Unfortunately, we do not have measurements of the amount of laser light absorbed by the target for this particular set of experiments. (Though for later data these measurements were carefully made - see table 4.1.) [74] Although this is an assumption, the details of the plasma initial condition do not critically affect the simulation results because the deposited energy quickly diffuses cylindrically into the bulk of the material. [75] Any reasonable initial thermal profile will work and give very similar results. Consequently, we ignore the subtle effects of different laser absorption mechanisms and simply state that the laser energy *is* absorbed by the material. Since there are many different laser absorption mechanisms, [76, 77, 78, 79, 80, 81, 82] and because the experiments do not differentiate between different mechanisms [83], this is the only valid option. The temperature profile in the material $T_e(r, z, t)$ is computed by numerically solving the diffusion

equation. [71, 72] In cylindrical geometry, the diffusion equation is:

$$\frac{d(c_p T_e)}{dt} = \frac{d\left(\kappa_r \frac{dT_e}{dr}\right)}{dr} + \frac{\kappa_z \frac{dT_e}{dr}}{dz}, \tag{4.1}$$

where $c_p(T_e)$ and $\kappa_{r,z}(T_e)$ are the temperature dependent heat capacity and diffusion coefficients, respectively. The average ionization state of the plasma and its heat capacity are computed by iteratively solving the Saha ionization equilibrium equation [84, 36, 40, 71] for each ionization level. [85] The diffusion coefficient $\kappa_{r,z,T}$ is the sum of the collisional and radiative diffusivities, κ_{SH} and κ_{rad}. For plasma temperatures $T < 100$ eV the collisional diffusion coefficient dominates. This is given by the Spitzer-Härm [38, 39, 36, 42] model of Coulomb collisions:

$$\kappa_{SH} = 1.96 \times 10^{-9} \frac{T_e^{5/2}}{Z \ln \Lambda}, \tag{4.2}$$

in [SI] units where Z is the ionization state and $\ln \Lambda$ is the Coulomb logarithm. For temperatures $T_e \geq 100$ eV, radiative transport dominates [36, 42] over Coulomb collisions. In this regime the radiative diffusivity κ_{rad} is:

$$\kappa_{rad} = \frac{16}{3} \sigma_{SB} T_e^3 \lambda_{Rosseland}, \tag{4.3}$$

where σ_{SB} is the Stefan-Boltzmann constant and $\lambda_{Rosseland}$ is the Rosseland radiation mean free path [44, 36, 86]:

$$\lambda_{Rosseland} = 1.2 \times 10^{19} \frac{T_e^2}{Z^2 n_i}, \tag{4.4}$$

n_i is the ion density in [m^{-3}] and T_e is temperature in eV.

Because of the combination of high plasma temperature and small spatial

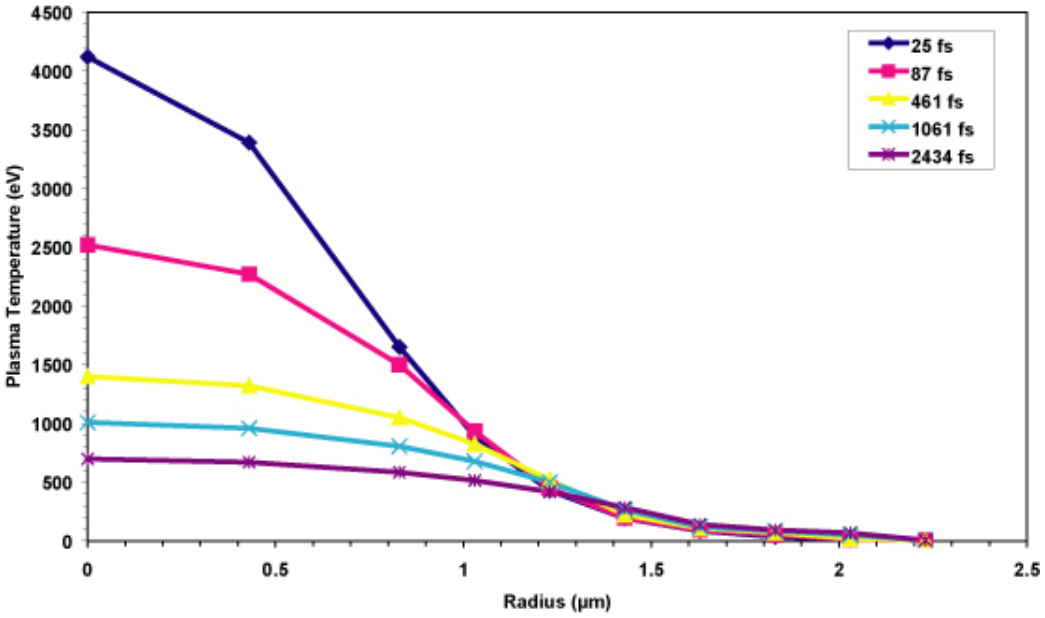

Figure 4.6: Calculation of plasma energy transport dominated by radiative diffusion for a plasma excited at 10^{18} W/cm^2 (0.88 mJ absorbed on target).

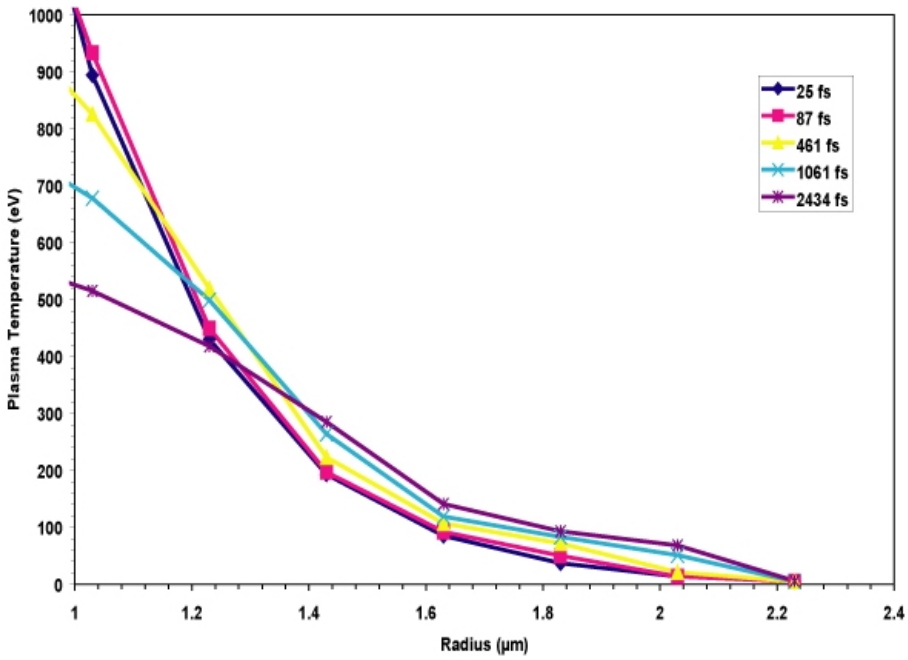

Figure 4.7: Zoom in on the expanding edge details for plasma energy transport dominated by radiative diffusion for a plasma excited at 10^{18} W/cm^2 (0.88 mJ absorbed on target).

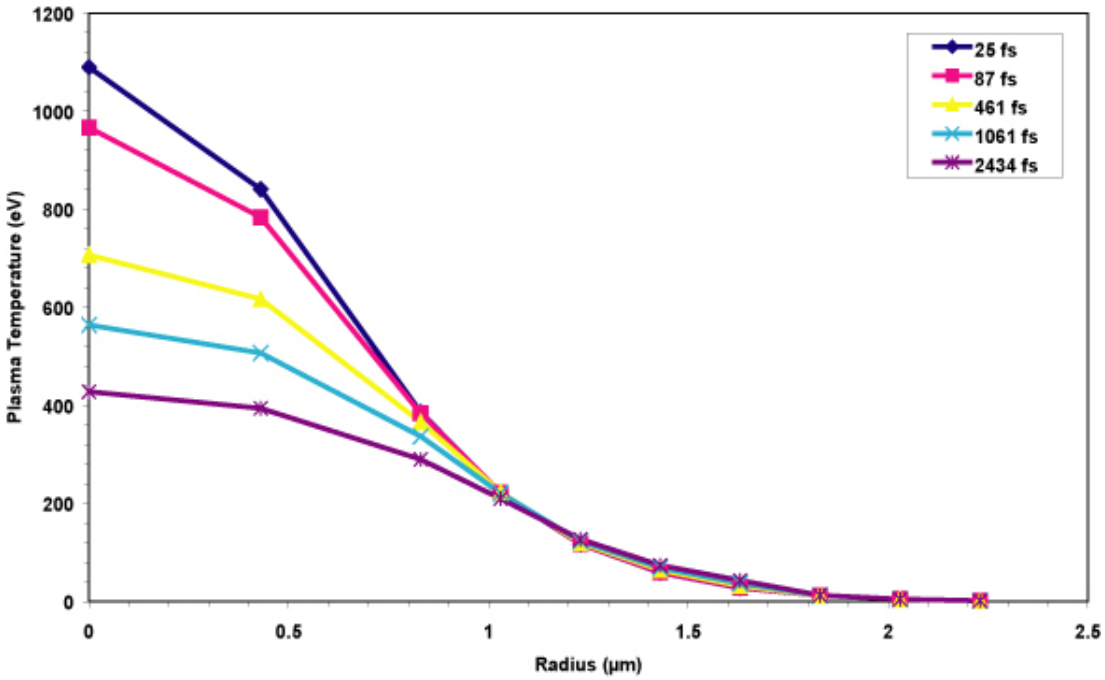

Figure 4.8: Calculation of plasma energy transport dominated by radiative diffusion for a plasma excited at 10^{17} W/cm^2 (0.20 mJ absorbed on target).

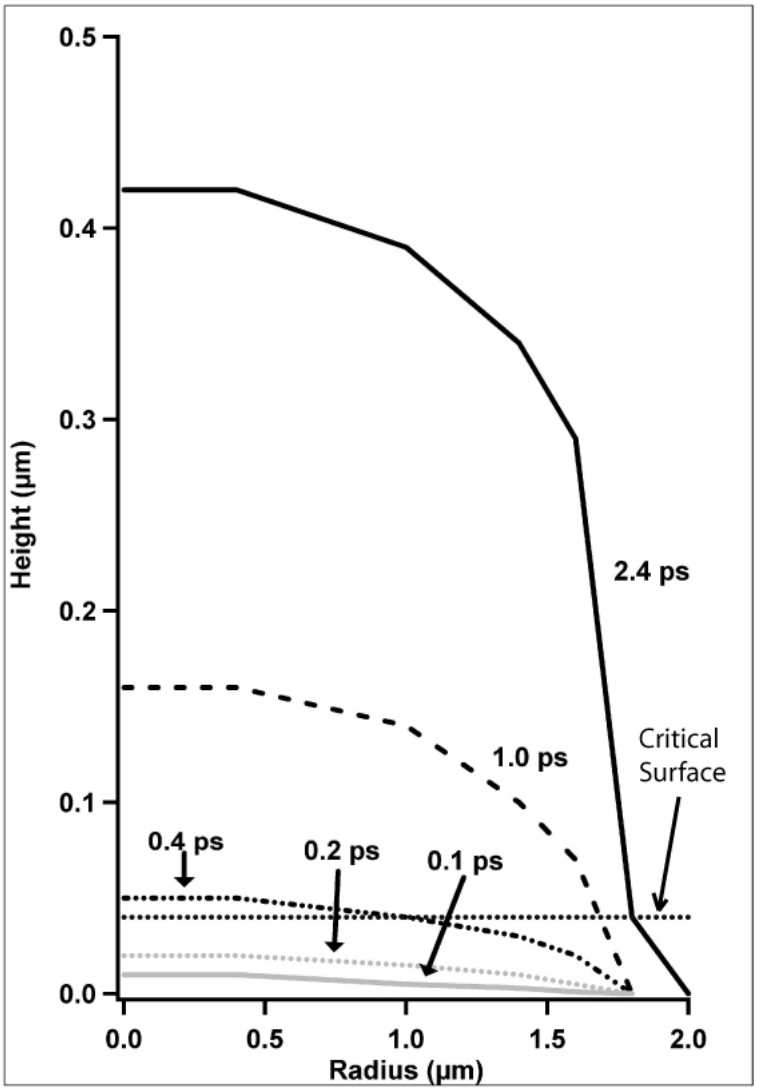

Figure 4.9: Time series showing vertical expansion of the heated plasma into vacuum computed with 1-D hydrodynamic simulation.

extent of the heated region, we must consider non-local radiative transport. [87, 88, 89] Radiation emitted from the heated plasma may travel farther than the extent of the heated region before colliding with the target material and depositing energy. For temperatures of interest in these experiments, the radiative mean free path $\lambda_{Rosseland} > 1$ μm. We approximately account for ballistic energy transport by assuming that thermal photons emitted in the heated plasma at position (r_0, z_0) are reabsorbed at position (r, z) with probability

$$w(r,z) = \frac{rr_0}{\lambda_{Rosseland}} \exp\left[\frac{-(r - r_0 + z - z_0)}{\lambda_{Rosseland}}\right] drdz. \tag{4.5}$$

Please note that $\int w(r,z)drdz = 1$ as required. Figure 4.7 shows the differences in the extent of heat propagation when including this non-local radiative transport approximation. The differences are small for distances $r < 2$ μm. For distances 2 μm $< r < 4$ μm the plasma temperature increases by several eV. This small increase in temperature is enough to increase the amount of plasma produced, which increases the plasma area that we observe with our resonantly absorbed 400 nm probe beam.

Calculation of the Expanding Plasma Density $n_e(r, z, t)$

To determine the z-expansion of the heated plasma into vacuum and the position of the plasma critical surface, we use a 1-D self-similar plasma hydrodynamic description. [90, 36, 40, 6] Although more detailed hydrodynamic models exist [91], it is not necessary to use them here because the plasma does not extend very far into vacuum. For conditions of the experiment, the expanding plasma has a large, density-independent thermal conductivity and low thermal capacity. In the hydrodynamic model we compute the vertical plasma expansion ($\hat{z}$) over several steps in radius r and ignore any transverse temperature gradients. Since the expanding

plasma does not travel far from the position of the unheated material over a few picoseconds (see figures **??** and 6.2), limiting the analysis to 1-D calculations should not introduce significant discrepancies with a full 3-D calculation over timescales of interest. The savings in computational time and complexity, though, are significant. We are interested in knowing the position of the plasma critical surface (for $\lambda_{probe} = 400$ nm) since that is where the probe beam is resonantly absorbed. Consequently the "critical position" $z_c(r,t)$ is calculated. The plasma density is

$$n(r,z,t) = n_0 \exp\left[-\frac{1+z}{c_s t}\right], \tag{4.6}$$

where n_0 is the surface plasma density and c_s is the temperature-dependent ion sound speed. [92, 90]

$$c_s = \left(\frac{ZT_e}{m_i}\right)^{1/2} \tag{4.7}$$

The plasma front expands outward into vacuum as $z_{front} = \alpha c_s t$. From this, the position of the plasma critical density surface $z_c(r,t)$ is computed. (See figure 4.9).

Determination of the Location of the Plasma Critical Surface $z_{crit}(r, n_e, t)$

In the experiments resonance absorption (RA) of the probe beam ($\lambda_{probe} = 400$ nm center wavelength) is used to observe the location of the heated, expanding plasma region. To analyze this we follow the typical 1-D RA theory. [43] From this analytic theory, the fractional absorption f_a of an obliquely incident, $P-$polarized laser beam by a linear plasma density distribution is given by:

$$f_a = 2.645\tau^2 \exp\left[-\frac{4}{3}\tau^3\right], \tag{4.8}$$

where

$$\tau = \left(\frac{\omega}{c} \frac{n_c}{\left(\frac{dn}{dz}\right)_{n_c}} \right)^{1/3} \sin\theta \tag{4.9}$$

and θ is the beam incidence angle, ω is the optical frequency and c the speed of light. [71, 72] Because of the excellent peak-pedestal contrast ratio of the λ^3 laser system ($> 1 : 10^{-5}$ for early experiments, $> 1 : 10^{-11}$ in later measurements), an exponential density ramp is more realistic for timescales of interest. For parameters of this experiment $\lambda_{probe} = 400$ nm, the critical density is $n_c = 7 \times 10^{27}$ m^{-3}. Calculating the β factor [43] for the evanescent wave incident on an exponential density ramp gives $\tau_{exp} = 1.166\tau_{Kruer,linear}$. Figure 4.9 shows the time evolution of this scenario. We compare this computation with our measurements by computing the time $t_{R=50\%}$ where the increasing absorption of the probe beam reaches 50% of incident probe light.

Further details regarding diffusive transport calculation

Program `DIFZAL.BAS` [73] solves the thermal diffusion equation. This equation relates the change in energy with time. One can write down the diffusive change in energy with time as:

$$\frac{dE}{dt} = \frac{d}{dy}\left(\kappa \frac{dT}{dy}\right) + \frac{1}{r}\frac{d}{dr}\left(\kappa \frac{dT}{dr}\right). \tag{4.10}$$

This is for cylindrical geometry where κ is the thermal conductivity. Remember that κ is a function of temperature T, so $\frac{dE}{dt}$ can be expanded:

$$\frac{dE}{dt} = \frac{d\kappa}{dy}\frac{dT}{dy} + \kappa(T)\frac{d^2T}{dy^2} + \kappa(T)\left[\frac{d^2T}{dr^2} + \frac{1}{r}\frac{dT}{dr}\right]. \tag{4.11}$$

In the simulation, the following values are used for the specific heat at constant pressure c_P:

$$c_P = 33 \pm 2 \text{ [m}^2 \text{ s}^{-2} \text{ eV}^{-1}\text{] for } T_e \geq 250eV, \tag{4.12}$$

$$c_P = 2.08 \times 10^{0.6} \text{ [m}^2 \text{ s}^{-2} \text{ eV}^{-1}\text{] for } T_e \leq 250eV, \tag{4.13}$$

These numbers are a fit to the specific heat calculated separately. The thermal conductivity is given by:

$$\kappa_{SH}(T_e) = \frac{3.17 \times 10^4 T_e^{5/2}}{Z^{0.44} ln\Lambda} \quad \text{for} \quad T_e \geq 20 \text{ eV}, \tag{4.14}$$

as such

$$\kappa_{SH}(T_e) = 2.6 \times 10^6 T_e \quad \text{for} \quad T_e \leq 20 \text{ eV}. \tag{4.15}$$

This result is just the electron coulomb-collisional thermal conductivity [71, 72, 37, 93, 36, 40] discussed previously. The ionization state is computed by:

$$Z = \frac{13 T_e}{T_e + 125} \text{ for } T_e \text{ in eV}. \tag{4.16}$$

This is a semi-empirical formula that is also a fit to the results given by `CORAL.BAS`, discussed later. The number of atoms *per cubic meter* is given as $n_d = 6 \times 10^{28}$ m^{-3} and the number of electrons is $n_e = Z n_d$. This is simply solid density for aluminum.

The initial temperature distribution in eV is described by a Gaussian:

$$T_e(\mathtt{k}, \mathtt{m}) = 0.1 + T_o \exp\left(\frac{-(2\mathtt{k}^2 + \mathtt{m}^2)}{\mathtt{mv}^2}\right), \tag{4.17}$$

where

$$\mathtt{mv} = \mathtt{INTEGER}\left[\frac{r_v}{r_o}\mathtt{mm}\right], \tag{4.18}$$

r_v is the laser spot radius in meters, r_o is the limit of the radial extent in meters, `mm` is the number of steps to divide r_o into, and `k` and `m` are the computational step indices in the radial and vertical directions, respectively. As a check, the energy content of the system is computed for each time step. Conservation of energy requires that the total energy remain constant between each time step. The energy is given by:

$$E = \int_{y_0}^{y_n} \int_{r}^{r_o} 2\pi e(r', y') r' dr' dy'. \tag{4.19}$$

Recall that the Spitzer-Härm thermal conductivity κ_{SH} as [71, 36, 42, 38, 39]:

$$\kappa_{SH} = \frac{4k_b(k_b T_e)^{5/2}}{m_e^{1/2}(Z+1)e^4 \ln \Lambda}, \tag{4.20}$$

where m_e is the electron mass, e is the electron charge, $k_b T_e$ is the electron thermal energy and $ln\Lambda$ is the Coulomb logarithm. The radiative thermal conductivity is described as:

$$\kappa_{rad} = \frac{16}{3}\sigma T_e^3 \lambda_R \tag{4.21}$$

where σ is the Stefan-Boltzmann constant and λ_R is the Rosseland (radiation) mean free path. For an ionized, hydrogenic plasma the Rosseland factor is approximately $\lambda_R \approx 9 \times 10^6 T_e^2 / Z^2 n_i$. [36, 42]

4.1.3 Calculating the diffraction and interference effects

In the first sets of data, the probe beam imaging system was not optimized for best imaging of the micrometer-scale plasma. This resulted in features of significant diffraction developing. Also, the diffraction may be due to reflection of the probe off of a spherical, expanding plasma surface. This reflection causes the probe light to spread out beyond the clear aperture of the primary $f/2$ imaging optic. This effect is

not observed in later, better data primarily because of the tremendous improvements in the laser system pulse contrast ratio. Please recall that for the first experiments, the laser contrast ratio was only $1 : 10^{-5}$. This was dramatically improved to better than $1 : 10^{-9}$ for the later data. This small pulse contrast ratio allowed a significant pre-plasma to develop. Also, in later experiments, much more time was invested in aligning the probe beam imaging system as well as possible (weeks instead of half a day). The Author believes that this substantial time investment was well-worth the result.

We are trying to image an object that varies in size between 1 μm and ≤ 50 μm with a primary lens of 25 mm clear aperture. It is extremely difficult to analyze this with a 2-D numerical calculation [94, 95] because the same sampling scale used for the object must also be used for the imaging lens hard aperture. So, if 10 pixels are used to represent the 1 micron object, then approximately 25000 pixels must be used to represent the 1 inch diameter hard aperture. This is far too large to give a reasonable computation time.

The primary equation for Fresnel-Kirchoff diffraction theory is:

$$U(P) = -\frac{Ai}{2\lambda} \int_{\mathcal{A}} \frac{e^{ik(r+s)}}{rs} \left[\cos(n, r) - \cos(n, s)\right] dS \tag{4.22}$$

We may apply the experimental parameters and solve the integral to gain insight into diffraction features observed in the data. The calculated result, made by convolving the interference calculation with the expanding critical surface position, is shown in Figure 4.10. We find that the resulting computation matches the diffraction features evident in our data quite well. [69]

The theory used in the calculations presented in this paper comes from the book by Born and Wolf [35] §8.6.3(b) – *Abbe Theory*. The example presented in

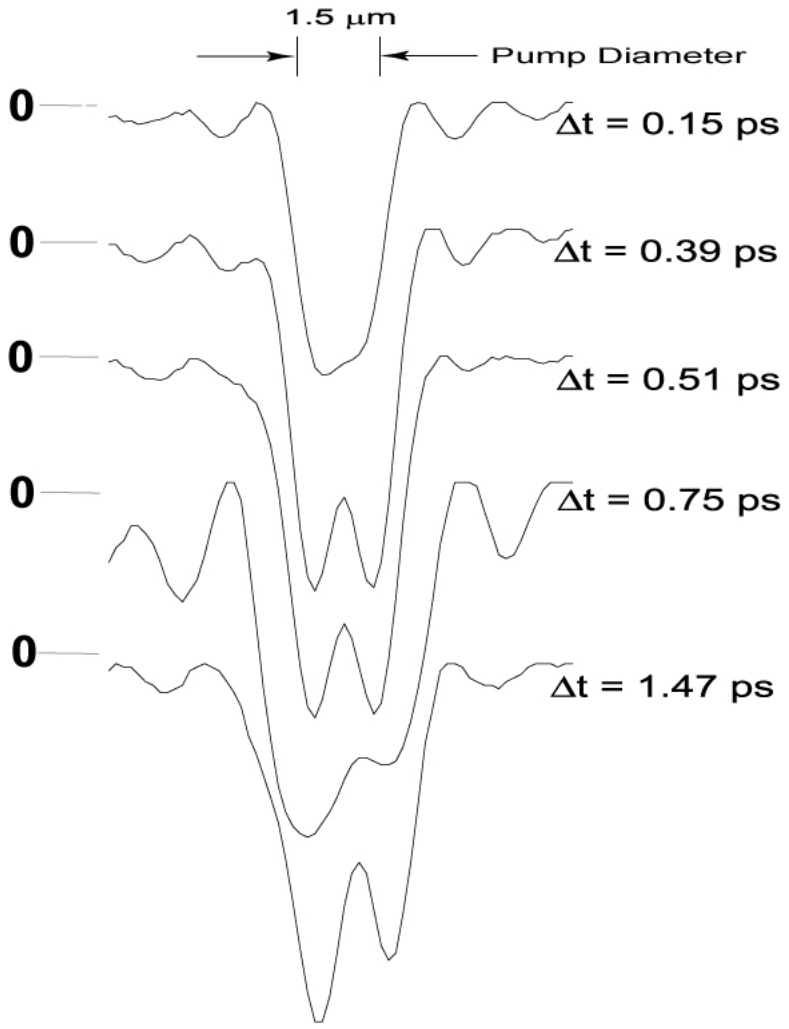

Figure 4.10: Calculation of diffraction features in the probe beam (λ_{probe} = 400 nm), observed through an $f/2$ primary imaging optic, at different probe beam delay times. These calculations take into account the radial and vertical expansion of the heated plasma, the absorption of the probe beam by the plasma, and the hard aperture of the imaging optic. [H. Langhoff, Private Communication (2004, 2005). Bowes *et. al.*, Optics Letters **31**, 116 (2006)]

§8.6.3(b) is for the special case where the object is at the focal distance in front of the imaging lens. We calculate the Fraunhofer diffraction pattern of the object propagated to the image plane.

$$U(\xi,\eta) = C_1 \int_{\mathcal{A}} F(x,y) e^{-ik\left(\frac{\xi}{f}x + \frac{\eta}{f}y\right)} dxdy, \tag{4.23}$$

where $\mathcal{A}$ is the aperture in the object plane. Also,

$$V(x',y') = C_2 \int_{\mathcal{B}} U(\xi,\eta) e^{-ik\left(\frac{x'}{D'}\xi + \frac{y'}{D'}\eta\right)} d\xi d\eta, \tag{4.24}$$

where $\mathcal{B}$ describes an aperture in the focal plane of the lens. The aperture $\mathcal{B}$ in the focal plane is equivalent to the aperture of the lens *in the plane of the lens.*

$$V(x',y') = C_2 \int_{\mathcal{A}} \int_{\mathcal{B}} F(x,y) e^{-ik\left[\left(x + \frac{f}{D'}x'\right)\xi + \left(y + \frac{f}{D'}y'\right)\eta\right]} dxdyd\xi d\eta \tag{4.25}$$

Here we calculate the diffraction from a wavelength sized hole propagated through a single lens to an image plane. The physical parameters used in this calculation are the same as in the λ^3 Experiment in Michigan.

Begin with equation (4.25) shown previously. Set the constants C_1 and C_2 to be 1. Physically these constants contain the information of the magnitude of the incoming electric field E_0 and its plane wave nature. Take the object function $F(x,y)$ to be a fully transparent circular hole in an opaque, infinitly conducting plane. Be aware, however, that in the actual experiment $F(x,y)$ is an opaque disk on a "fully transmissive" background. To understand and solve the latter case one must use *Babinet's Principle* [35].

First solve for $U(\xi,\eta)$ then for $V(x',y')$. Converting to polar coordinates: So:

Table 4.2: Conversion from cartesian to polar coordinates used in the analytic calculation of diffraction features observed in the experiments.

Location	$\hat{e}_1$	$\hat{e}_2$
Object Plane	$x = \rho\cos\theta$	$y = \rho\sin\theta$
Back Focal Plane	$\xi = r\cos\phi$	$\eta = r\sin\phi$
Image Plane	$x' = l\cos\psi$	$y' = l\sin\psi$

$$U(r,\phi) = \int_{\mathcal{A}} F(\rho,\theta) e^{\{-i\frac{k}{f}[r\cos\phi\rho\cos\theta + r\sin\phi\rho\cos\theta]\}} \rho d\rho d\theta. \tag{4.26}$$

Recall that $\cos(A \pm B) = \cos A\cos B \mp \sin A\sin B$ and:

$$U(\rho,\theta) = \int_{\mathcal{A}} F(\rho,\theta) e^{-i\frac{kr\rho}{f}\cos(\theta-\phi)} \rho d\rho d\theta. \tag{4.27}$$

Set the object $F(\rho,\theta)$ to be a step function

$$F(\rho,\theta) = \begin{pmatrix} 1 \text{ for } 0 \le \rho \le a \\ 0 \text{ else} \end{pmatrix}. \tag{4.28}$$

So:

$$U(\rho,\theta) = \int_0^a \int_0^{2\pi} e^{-i\frac{kr\rho}{f}\cos(\theta-\phi)} \rho d\rho d\theta. \tag{4.29}$$

Recall the integral form of the Bessel Function $J_n(x)$:

$$J_n(x) = \frac{i^{-n}}{2\pi} \int_0^{2\pi} e^{ix\cos\alpha} e^{in\alpha} d\alpha. \tag{4.30}$$

and the derivative relation:

$$\frac{d}{dx}[x^{n+1} J_{n+1}(x)] = x^{n+1} J_n(x) \tag{4.31}$$

Table 4.3: Parameters for analytic diffraction calculation for conditions of this experiment

Parameter	Symbol	Value Range
Radius of Probe Absorption Spot	a	0 to 3 μm
Imaging Lens Focal Length	f	50 mm
Imaging Lens Radius	b	12.5 mm
Probe Beam Wavelength	λ	400 nm
Distance from Focal Plane to Image Plane	D'	720 mm

Using these two relations with equation 4.29 yields:

$$\begin{aligned} U(\rho,\phi) &= 2\pi\int_0^a J_0(\frac{kr\rho}{f})\rho d\rho \qquad (4.32)\\ &= \frac{2\pi a^2 f}{kar}J_1(kar). \qquad (4.33)\end{aligned}$$

Now plug 4.32 into 4.24 (after converting 4.24 into polar coordinates) and solve:

$$\begin{aligned} V(l,\psi) &= \int_{\mathcal{B}}\frac{2\pi a^2 f}{kar}J_1(kar)\exp\left[-i\frac{klr}{D'}(l\cos\psi r\cos\phi + l\sin\psi r\sin\phi)\right]rdrd\phi\\ &= \int_0^b\int_0^{2\pi}\frac{2\pi a^2 f}{kar}J_1(kar)\exp\left[-i\frac{klr}{D'}\cos(\phi-\psi)\right]rdrd\phi\\ &= \int_0^b\frac{4\pi^2 a^2 f}{ka}J_1(kar)J_0\left(\frac{klr}{D'}\right)dr. \qquad (4.34)\end{aligned}$$

Equation 4.34 needs to be solved in order to obtain the field distribution in the image plane. This integration must be done numerically because an analytic solution of $\int J_1(ax)J_0(bx)dx$ is not known. Substituting $k=\frac{2\pi}{\lambda}$ into the constant term of 4.34 gives:

$$\frac{4\pi^2 a^2 f}{ka} = \frac{4\pi^2 a^2 f\lambda}{2\pi a} = 2\pi a f\lambda \qquad (4.35)$$

The experimental parameters that get plugged into 4.34 are: Plug in to get:

$$2\pi a f \lambda = 3.8 \times 10^{-4} \text{ mm}^3 \quad (4.36)$$

$$ka = 47.12 \text{ for } a = 3\ \mu\text{m} \quad (4.37)$$

$$= 7.85 \text{ for } a = 0.5\ \mu\text{m} \quad (4.38)$$

$$\frac{k}{D'} = 21.8 \text{ mm}^{-2} \quad (4.39)$$

4.2 Energy transport dominated by ballistic hot electrons

The most recent experiments made use of an improved λ^3 Laser system. The laser system provided > 1 mJ energy on target (even after splitting off 15% of the main pulse to form the 2ω probe pulse), with 800 nm (center), 35 fs pulses and temporal contrast ratio better than $1 : 10^{-9}$. These are significant improvements over the original system. In particular, the increased pulse contrast ratio means that there will be no formation of a pre-plasma on the solid targets. (When focusing to 10^{18} W/cm^2, the pre-pulses will be $\leq 10^9$ W/cm^2, which is lower than the intensity required to form a plasma.) Also, pulse energy measurements were made at the same location as the target rather than at some outside point as in the previous experiments. This means that the energy measurements are accurate for the amount of energy *incident on the target* rather than an overestimate. The previous measurements did not take into account energy losses as the pump beam was propagated off several metal mirrors and through chamber windows before reaching the target.

In these new experiments we have explored the effects of pump laser polarization and target atomic number Z (aluminum and copper targets) on dynamics of radial energy transport in the hot plasma. The pump laser beam is incident on the target at 45° for all data sets presented here. Additionally, all of these exper-

iments use a $P-$polarized, $\lambda = 400$ nm, 40 fs probe pulse incident on the target at $\theta_{probe} = 75^{\circ}$ from the normal. This probe pulse is focused to a large ≈ 120 μm diameter spot, completely filling the viewing window of the imaging CCD. Using an $S-$polarized probe pulse is unnecessary as we have already shown that we use resonance absorption of the probe beam to observe the hot plasma dynamics. Each data image is the sum of six (6) laser shots, because the CCD frame rate is 30 Hz and the laser repetition rate is 500 Hz. Due to the significant improvements in the laser system it is difficult to make direct, quantitative comparison of this new data with the results discussed previously. However, we may make strong qualitative comparison between the two experiments and draw firm conclusions from the new data itself.

First, we will look at the images shown in figure 4.11, which were taken with a $P-$polarized pump pulse at 10^{18} W/cm^2 on aluminum. When the probe beam arrives before the pump beam ($\Delta t < 0$), clean target surface is seen in the images. Mottling of the image is due to imperfections in the incident probe beam rather than the target. A bright 2ω spot is also present in the images. This is 2ω generated by the pump pulses on the target. Enough of this pump second harmonic is scattered into the probe imaging system to be detected by the CCD. The presence of this pump-generated 2ω signal is the greatest feature of the new data. This 2ω spot allows *direct* measurement of the focal spot size of the pump beam on the target. Unfortunately, the pixels in this region are saturated, so the pump size measurement will give an upper limit rather than a definite diameter.

As the pump and probe laser pulses arrive at the same time, a heated plasma region expands out from the pump spot. In these new data, the size of this heated region is tremendous compared to the size of the pump focal spot. The heated region

extends outward to 45 μm by $\delta t = 311$ fs for an expansion speed of 10^8 cm/s. As the pump and probe beams overlap in time, interference fringes appear in the image. These fringes are due to interference between the coherent pulses of pump-generated 2ω and the probe 2ω. Curvature of the fringes is because the pump-generated 2ω is strongly diverging (due to the $f/1$ pump focusing optic) while the probe beam is comparatively collimated. From these fringes we can measure the duration of the probe pulse fairly well.

Clearly, the radiative diffusion model (with non-local statistical enhancements) cannot reproduce the plasma expansion size and speed observed in these new data. We must conclude that the primary transport mechanism observed here is ballistic hot electrons. To that end, we have obtained particle-in-cell (PIC) calculations [96] for an aluminum target under conditions identical to the experiment. This result is shown in figure 4.19. These simulations show that the plasma should develop hot electrons with an average temperature up to 15 keV. The simulation suggests that the plasma should expand out to approximately 20 μm in width, which is comparable to the width we observe in the data. Notice that the electrons are confined to near the target surface outside of the heated hemisphere. This confinement is due to the strong self-generated magnetic fields present. Magnetic fields up to 2 MG are predicted for this experiment (see figure 4.20). However, the PIC simulations predict that we should observe strong asymmetry of the heated plasma region in the direction of pump laser pulse propagation. We do not observe such strong asymmetry in any the data, even for copper targets or different pump laser intensities. To fully model the plasma we observe in the experiments, it may be necessary to undertake a full relativistic Fokker-Planck multi-dimensional fluid simulation. [75] We have yet to locate a collaborator willing to accept such a challenging

project.

Figures 4.12 through 4.14 show plasma expansion on aluminum targets for intensities of 10^{18} W/cm^2 and 10^{17} W/cm^2, and for $P-$ and $S-$polarized pump beam. We observe little difference between transport from $P-$ or $S-$polarized pump beam at the same intensity. At 10^{17} W/cm^2, the observed expansion is reduced, and we no longer observe a pump-generated 2ω spot in the images. Figures 4.15 through 4.18 show data taken with copper targets excited at the same conditions as the aluminum targets. Radial transport is reduced in these data because of the increase in target atomic number ($Z_{aluminum} = 13$, while $Z_{copper} = 29$). There are now more electrons to heat and ionize with the same laser energy.

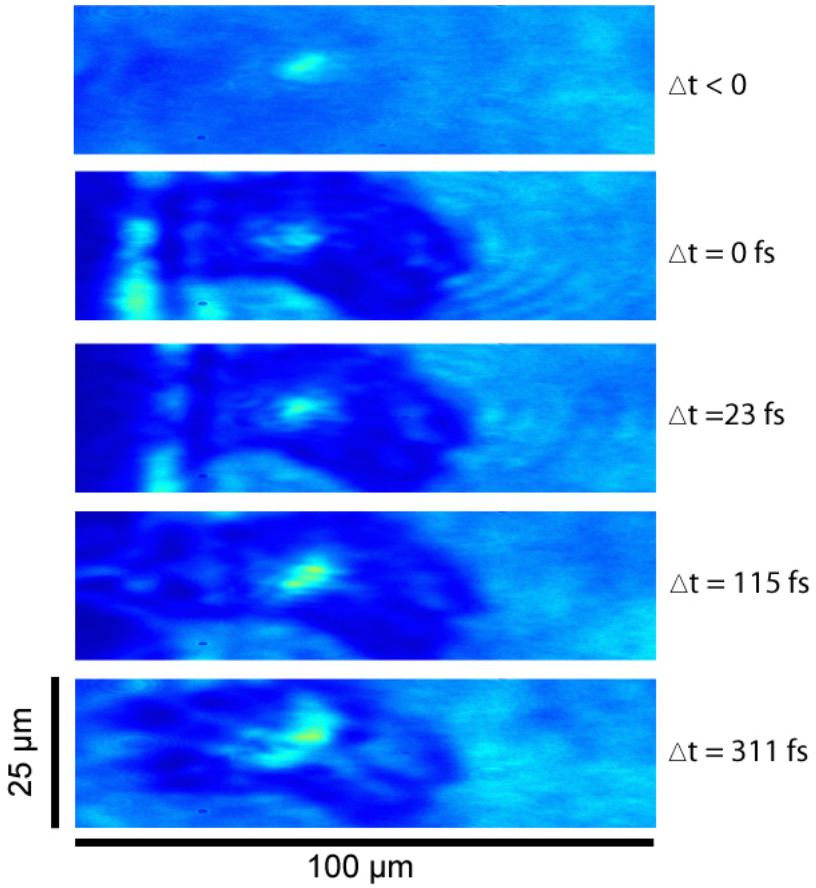

Figure 4.11: Images of the radially expanding aluminum plasma excited by a pump pulse of parameters ($I = 1.18 \times 10^{18}$ W/cm^2, $P-$polarized, 35 fs) at 45° incidence angle. The central bright region is pump-created 2ω light that leaks into the probe beam imaging system. The pump and probe beams interfere while they are temporally overlapped, giving rise to the fringe patterns observed at early probe delay times. Curvature of the fringes is because the pump-generated 2ω diverges much more strongly than the comparatively collimated probe beam. The plasma region expands out to a full width of 45 μm by $\Delta t = 311$ fs.

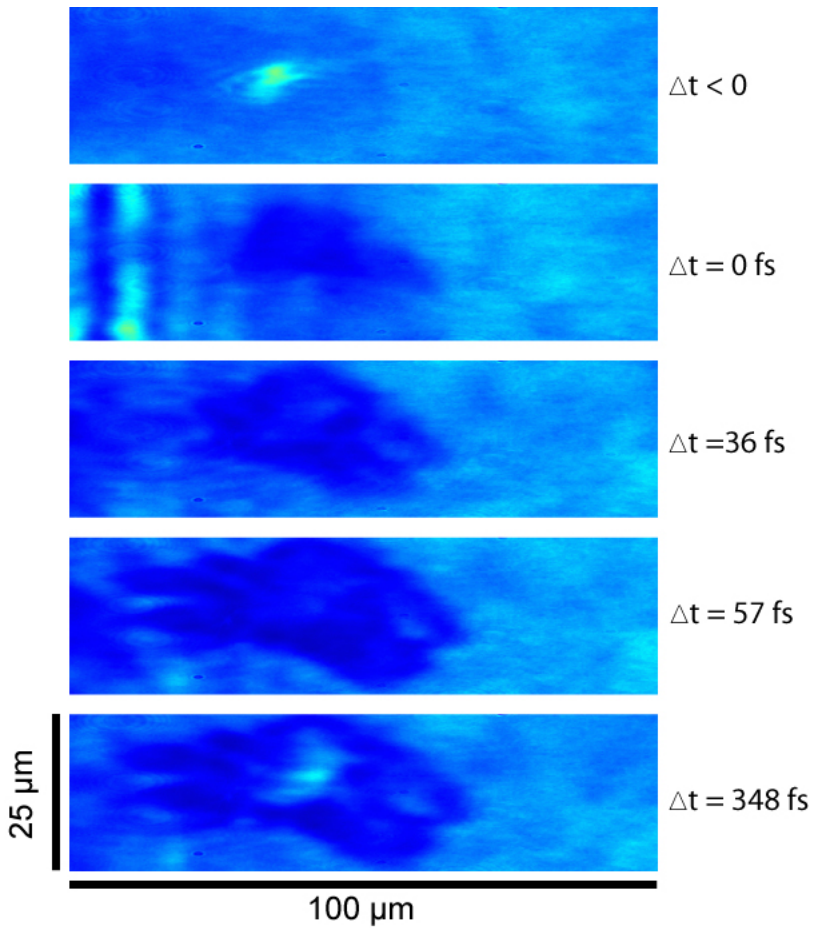

Figure 4.12: Images of the radially expanding aluminum plasma excited by a pump pulse of parameters ($I = 1.18 \times 10^{18}$ W/cm^2, $S-$polarized, 35 fs) at 45° incidence angle. The central bright region is pump-created 2ω light that leaks into the probe beam imaging system. The pump and probe beams interfere while they are temporally overlapped, giving rise to the fringe patterns observed at early probe delay times. Curvature of the fringes is because the pump-generated 2ω diverges much more strongly than the comparatively collimated probe beam.

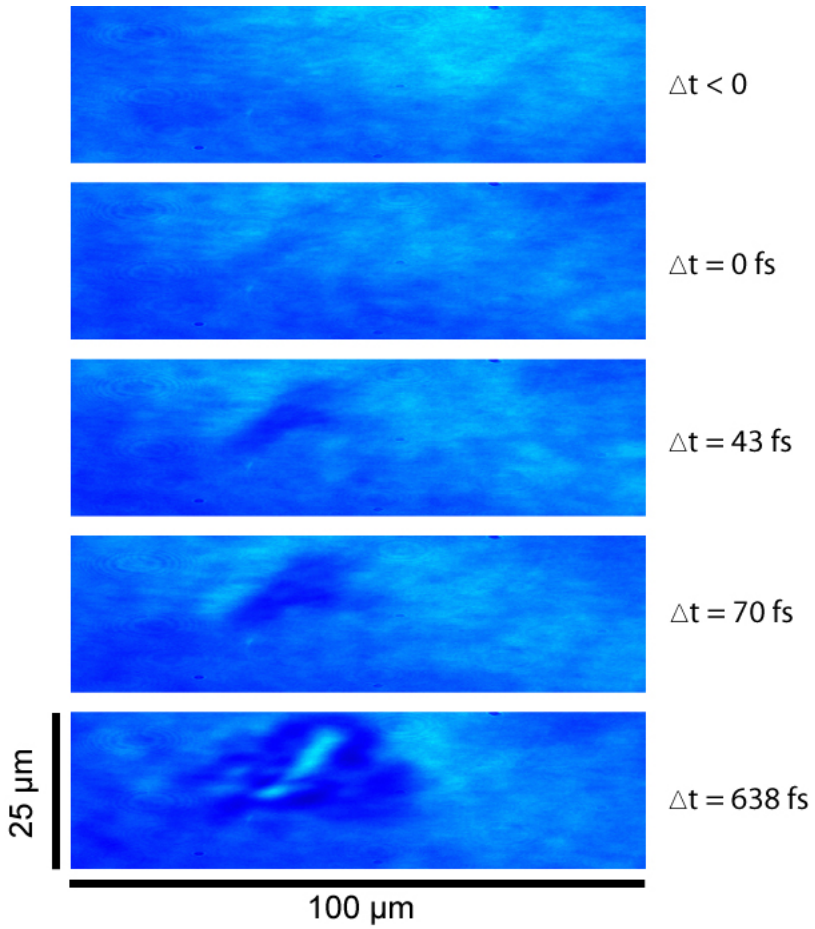

Figure 4.13: Images of the radially expanding aluminum plasma excited by a pump pulse of $I = 1.18 \times 10^{17}$ W/cm^2, $P-$polarized, 35 fs at 45° incidence angle. At this reduced pump intensity, the pump-generated 2ω is not bright enough to penetrate through the probe imaging system. The expansion in this excitation regime is driven predominantly by non-local radiative transport. At later probe delays a bright region appears at the center of the heated plasma. This region is where the plasma has expanded vertically into vacuum far enough for the probe beam to be reflected, rather than resonantly absorbed, by the underdense plasma.

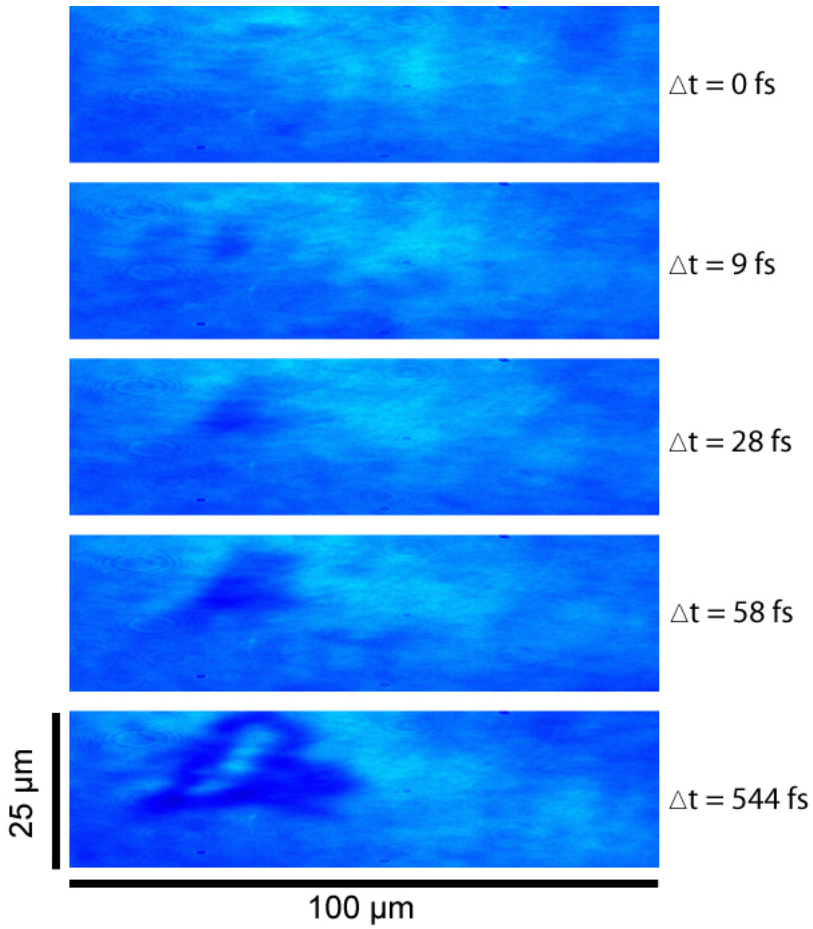

Figure 4.14: Images of the radially expanding aluminum plasma excited by a pump pulse of $I = 1.18 \times 10^{17}$ W/cm^2, $S-$polarized, 35 fs at 45° incidence angle. At this reduced pump intensity, the pump-generated 2ω is not bright enough to penetrate through the probe imaging system. The expansion in this excitation regime is driven predominantly by non-local radiative transport. At later probe delays a bright region appears at the center of the heated plasma. This region is where the plasma has expanded vertically into vacuum far enough for the probe beam to be reflected, rather than resonantly absorbed, by the underdense plasma.

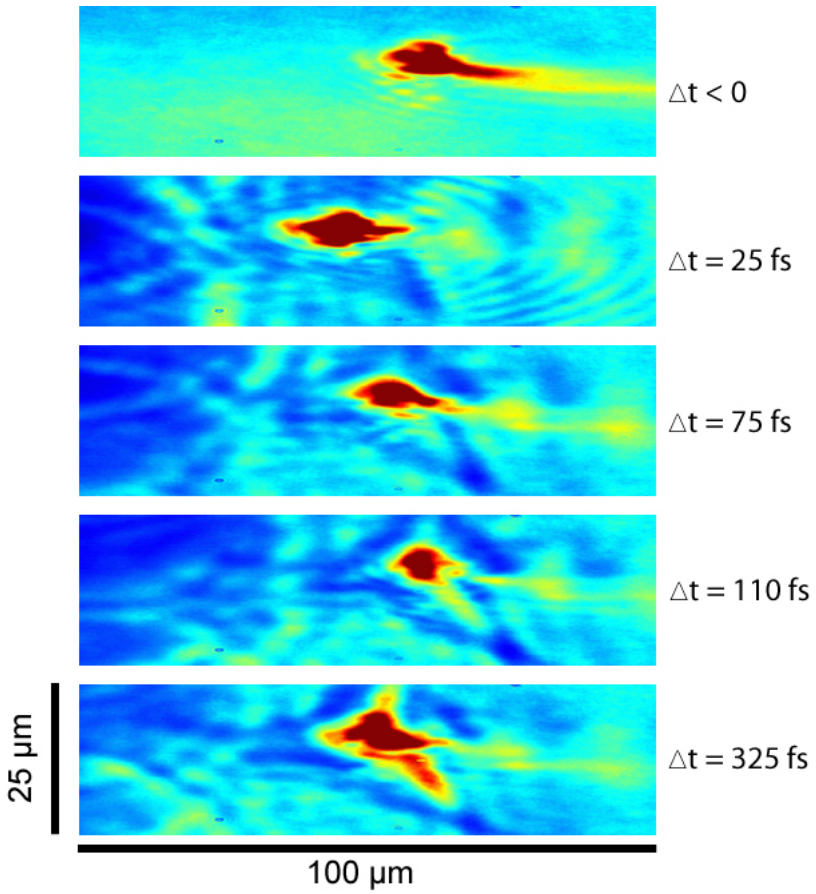

Figure 4.15: Images of the radially expanding copper plasma excited by a pump pulse of $I = 1.18 \times 10^{18}$ W/cm^2, $P-$polarized, 35 fs at 45° incidence angle.

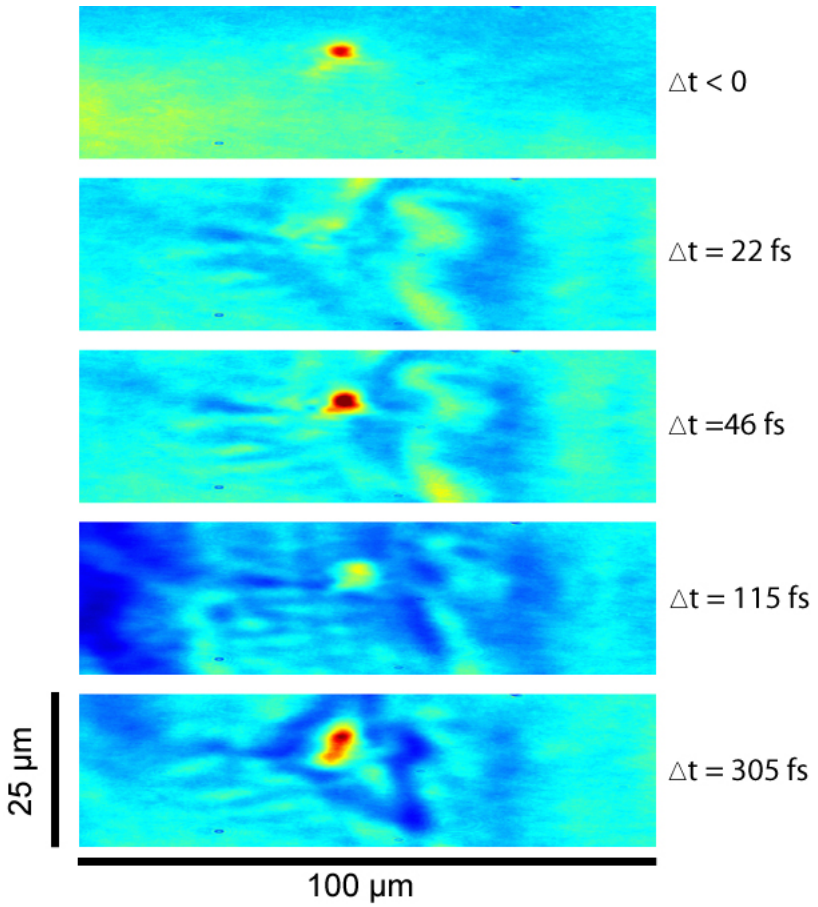

Figure 4.16: Images of the radially expanding copper plasma excited by a pump pulse of $I = 1.18 \times 10^{18}$ W/cm^2, $S-$polarized, 35 fs at 45° incidence angle.

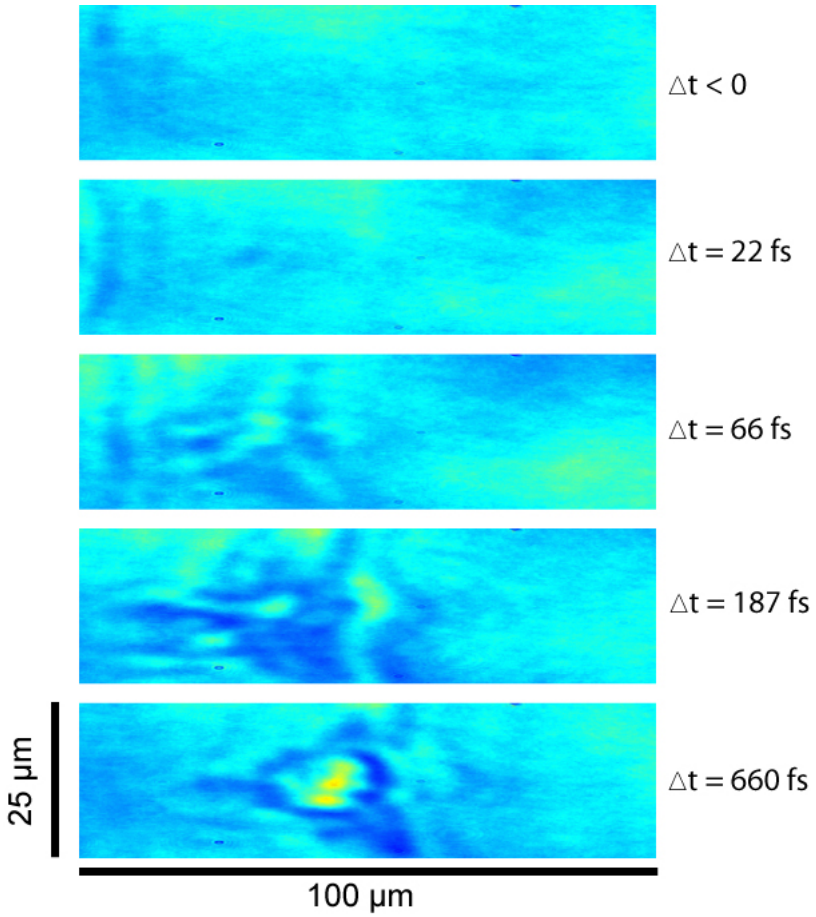

Figure 4.17: Images of the radially expanding copper plasma excited by a pump pulse of $I = 1.18 \times 10^{17}$ W/cm^2, $P-$polarized, 35 fs at 45° incidence angle.

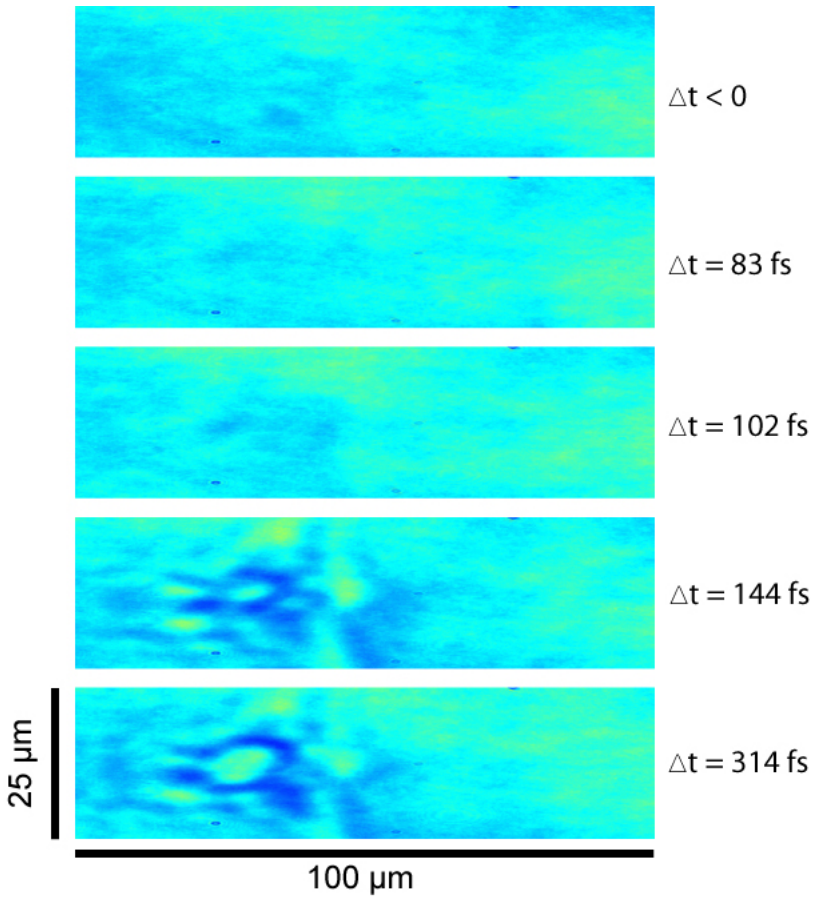

Figure 4.18: Images of the radially expanding copper plasma excited by a pump pulse of $I = 1.18 \times 10^{17}$ W/cm^2, $S-$polarized, 35 fs at 45° incidence angle.

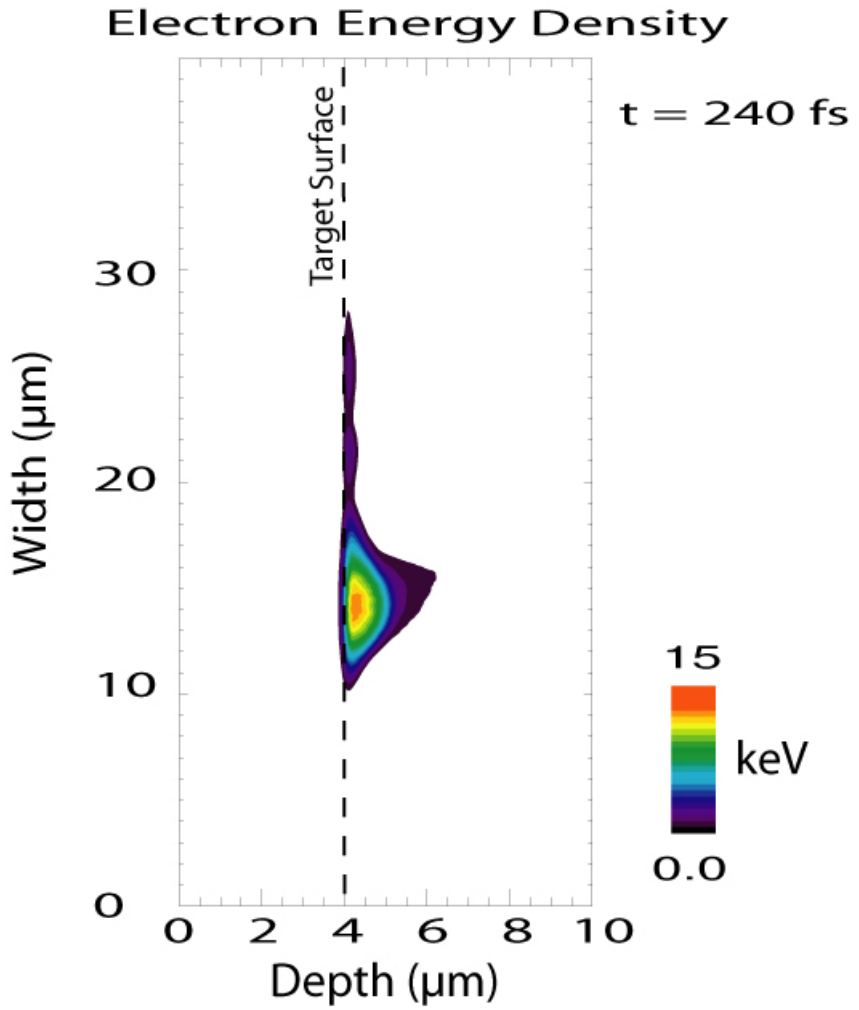

Figure 4.19: Electron energy density from particle-in-cell simulation for pump laser pulse conditions of $I = 1.18 \times 10^{18}$ W/cm^2, $P-$polarized, 35 fs at 45° incidence angle on solid density aluminum target. In this simulation the critical density $n_c = 1.56 \times 10^{21}$ cm^{-3}, electron density $n_e = 256 n_c$ and ion density $n_i = 25.6 n_c$. Electrons at the center of the pump laser pulse are heated to $T_e = 15$ keV. Lateral motion of the electrons are confined to the surface of the target by their self-generated magnetic fields. [Y. Sentoku, Private Communication (2005)]

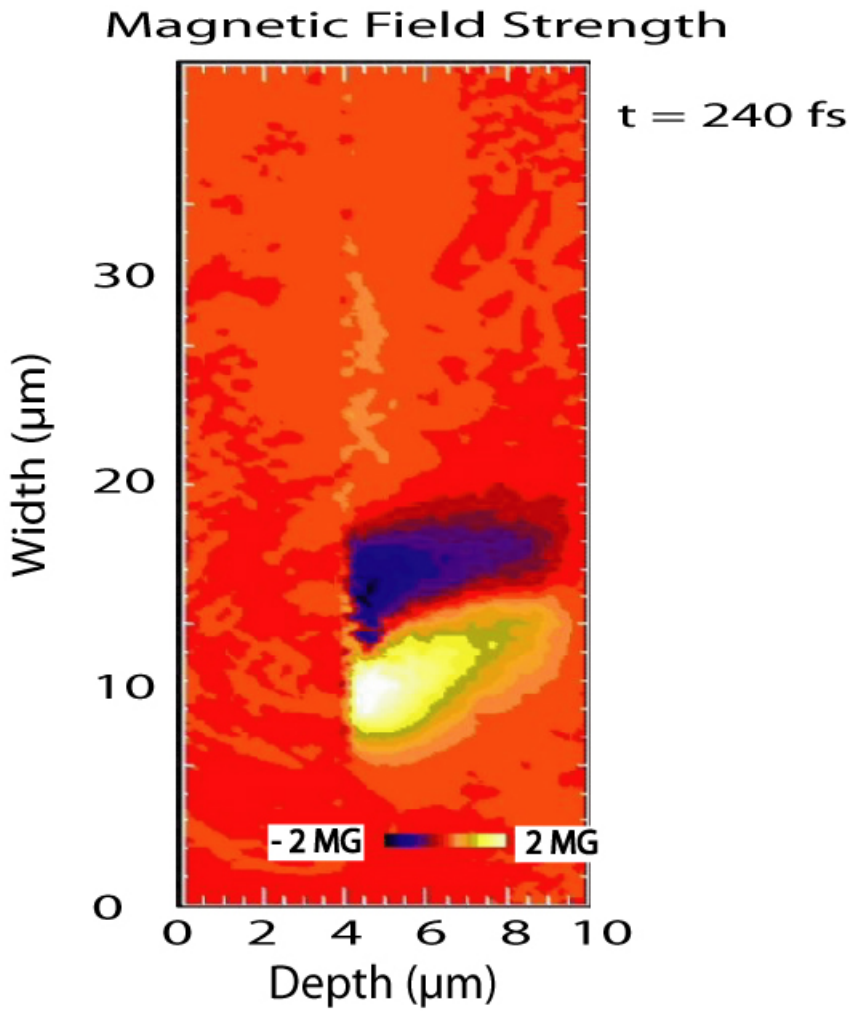

Figure 4.20: Magnetic field strength from particle-in-cell simulation for pump laser pulse conditions of $I = 1.18 \times 10^{18}$ W/cm^2, $P-$polarized, 35 fs at 45° incidence angle on solid density aluminum target. Magnetic fields, generated by the strong currents of ballistic hot electrons, up to ± 2 MG are predicted for these experimental conditions. [Y. Sentoku, Private Communication (2005)]

Chapter 5

Conclusion

In these experiments we have observed non-local energy transport by radiation and hot electrons in a micrometer-scale solid-density plasma. To observe and diagnose the plasma we use femtosecond microscopy techniques with a resonantly absorbed probe laser beam to record high spatial resolution images of the expanding plasma over the first picosecond after excitation by intense laser pump pulses. We analyze this energy transport by applying a 2-D radiative diffusion code and multidimensional particle-in-cell simulations. We find that the radiative diffusion code matches the overall expansion of the microplasma for early experiments, but does not adequately describe the non-local behavior of the energy transport. Later experiments, performed with a greatly improved laser system, show that hot electrons dominate the energy transport over the first picosecond of plasma expansion. We have modeled this transport by applying particle-in-cell simulations.

5.0.1 Suggestion for further work

An excellent follow-up experiment to this work would be to measure the magnitude and distribution of the megagauss self-generated magnetic fields in the microplasma. This can be done by using techniques such as frequency domain holography [97] to detect probe beam polarization changes due to the Cotton-Mouton effect within the plasma. The polarization changes expected are too small to be observed by conventional methods. [98] To that end, we make a calculation of the polarization rotation of a normally incident, 400 nm probe beam via the Cotton-Mouton effect in a magnetized plasma. [99, 100, 101, 102, 103, 104, 105, 106, 107, 108] General information about the calculation is given, and plots of the resulting polarization rotation are presented at the end of this section. The polarization rotation due to a few-megagauss magnetic field, in a few-micrometer thick plasma, will require very sensitive techniques to measure.

Chapter 6

Appendix

6.0.2 Brief Introduction to Plasma Birefringence

In order to measure the B-fields created in the microplasmas, we are interested in using the Cotton-Mouton effect and/or the Faraday effect. S. E. Segre analyzes these effects for cases where the fields are "large" in the paper "Plasma polarimetry for large Cotton-Mouton and Faraday effects", Phys. Plasmas **2**, 2908 (1995) [104].

The theory that Segre[104] uses involved, at some point, making a WKB approximation. Also, this theory is supposed to only be valid for when $\omega_p \ll \omega_{laser}$ and $\omega_{cyclotron} \ll \omega_{laser}$. In this experiment, we want to probe up to the critical density as far as possible, so $\omega_p \sim \omega_{laser}$. For magnetic fields of $\sim$ 2 MG, the cyclotron frequency is $\omega_{cyclotron} \sim 10^{14}$ s^{-1}, which is almost the laser frequency $\omega_{laser} = 1.15 \times 10^{15}$ s^{-1} for $\lambda = 400$ nm.

All of the analysis is done in terms of the Stokes parameters $\vec{s}_0$, which fully describe the polarization state of an electromagnetic (EM) wave. [35] We may also describe the polarization state of the EM wave by using a "polarization ellipse". The polarization ellipse is described by two parameters; ψ, the angle between the major

axis of the ellipse and the x-coordinate, and χ, the ratio of major and minor axis of the ellipse. The relationship between the Stokes parameters and the polarization ellipse is as follows:

$$s_1 = s_0 \cos 2\chi \cos 2\psi \tag{6.1}$$

$$s_2 = s_0 \cos 2\chi \sin 2\psi \tag{6.2}$$

$$s_3 = s_0 \sin 2\chi \tag{6.3}$$

$$s_0^2 = s_1^2 + s_2^2 + s_3^2 \tag{6.4}$$

So then $s_2/s_1 = \tan 2\psi$ and $s_3/\sqrt{1-s_3^2} = \tan 2\chi$.

6.0.3 The mathematics of Cotton-Mouton

To determine how the polarization changes in the birefringent plasma, we introduce $\mathbf{T}(Z)$, a dimensionless vector that describes the polarization state of the EM wave in a magnetized plasma. Here, $Z = z/a$ is a dimensionless length, where a is some characteristic length of the plasma, such as the gradient scale length, or the distance over which the magnetic field is large. The components of $\mathbf{T}(Z)$ are, in **cgs** units:

$$T_1 = \frac{a\omega_p^2}{2c\omega^3}\left(\frac{e}{m_e c}\right)^2 (B_y^2(Z) - B_x^2(Z)), \tag{6.5}$$

$$T_2 = -\frac{a\omega_p^2}{2c\omega^3}\left(\frac{e}{m_e c}\right)^2 B_y(Z)B_x(Z), \tag{6.6}$$

$$T_3 = \frac{a\omega_p^2}{2c\omega^2}\left(\frac{e}{m_e c}\right) B_z(Z), \tag{6.7}$$

where ω_p is the plasma frequency, ω is the frequency of the EM wave, e is the electron charge, m_e is the electron mass, and the magnetic field $\mathbf{B}(Z)$ is described in component form as $\mathbf{B}(Z) = B_x(Z) + B_y(Z) + B_z(Z)$. T_1 and T_2 give the Cotton-

Mouton effect, and T_3 is responsible for the Faraday effect. Jumping a few steps (which are described further in Segre[104]), the polarization state of an EM wave after propagating through a magnetized plasma is given by

$$\vec{s}_f = \mathbf{M}_{jk}(Z_1) \cdot \vec{s}_i \tag{6.8}$$

where $\mathbf{M}_{jk}(Z_1)$ is the polarization transition matrix. Segre states that for small plasma effects $\mathbf{M}_{jk}(Z_1)$ may be written as

$$\mathbf{M}_{jk}(Z_1) = 1 + \mathbf{M}_{jk}^{(1)} + \mathbf{M}_{jk}^{(2)} + \ldots. \tag{6.9}$$

Unfortunately, Segre does not define what is meant by "small plasma effects" or "large plasma effects". To continue, presume that any polarization rotation effects in our microplasma are small, simply because the scale size of the plasma is so small. The lowest order matrices $\mathbf{M}_{jk}^{(1)}$ and $\mathbf{M}_{jk}^{(2)}$ are

$$\mathbf{M}_{jk}^{(1)} = \begin{bmatrix} 0 & -W_3 & W_2 \\ W_3 & 0 & -W_1 \\ -W_2 & W_1 & 0 \end{bmatrix}, \tag{6.10}$$

$$\mathbf{M}_{jk}^{(2)} = \begin{bmatrix} -(W_{22}+W_{33}) & W_{21} & W_{31} \\ W_{12} & -(W_{33}+W_{11}) & W_{32} \\ W_{13} & W_{23} & -(W_{11}+W_{22}) \end{bmatrix}, \tag{6.11}$$

where the matrix elements W are

$$W_j = \int_{Z_i}^{Z_f} T_j(Z)dZ \tag{6.12}$$

$$W_{jk} = \int_{Z_i}^{Z_f} T_j(Z)dZ \int_{Z_i'}^{Z_f'} T_k(Z')dZ' \tag{6.13}$$

If $\vec{s}_i$ is

$$\vec{s}_i = \begin{bmatrix} s_i^{(1)} \\ s_i^{(2)} \\ s_i^{(3)} \end{bmatrix}. \tag{6.14}$$

Then

$$\begin{aligned} \vec{s}_f &= \vec{s}_i + \mathbf{M}_{jk}^{(1)} \cdot \vec{s}_i + \mathbf{M}_{jk}^{(2)} \cdot \vec{s}_i \qquad (6.15) \\ &= \begin{bmatrix} s_i^{(1)} + s_i^{(3)}W_2 + s_i^{(2)}W_{21} - s_i^{(2)}W_3 + s_i^{(3)}W_{31} - s_i^{(1)}(W_{22} + W_{33}) \\ s_i^{(2)} + s_i^{(3)}W_1 + s_i^{(1)}W_{12} - s_i^{(1)}W_3 + s_i^{(3)}W_{32} - s_i^{(2)}(W_{11} + W_{33}) \\ s_i^{(3)} + s_i^{(2)}W_1 + s_i^{(1)}W_{13} - s_i^{(1)}W_2 + s_i^{(2)}W_{23} - s_i^{(3)}(W_{11} + W_{22}) \end{bmatrix}. \end{aligned}$$

6.0.4 Application to our Experiment

What do the magnetic fields in our microplasma look like, and what do we know or assume to know about that plasma? From particle-in-cell simulations by Sentoku [96], we know that a magnetic field loop, centered around the pump laser focal spot, is created by the motion of fast electrons driven by the intense pump laser pulse. For an aluminum target and pump laser incidence angle of 45° from the normal, these fields may have magnitude up to 2 MG, and up to 5 MG for a normally incident pulse on carbon targets. [96]

Are these high magnetic fields measurable with an optical probe? Let us consider a probe laser pulse normally incident to the target. With such a probe,

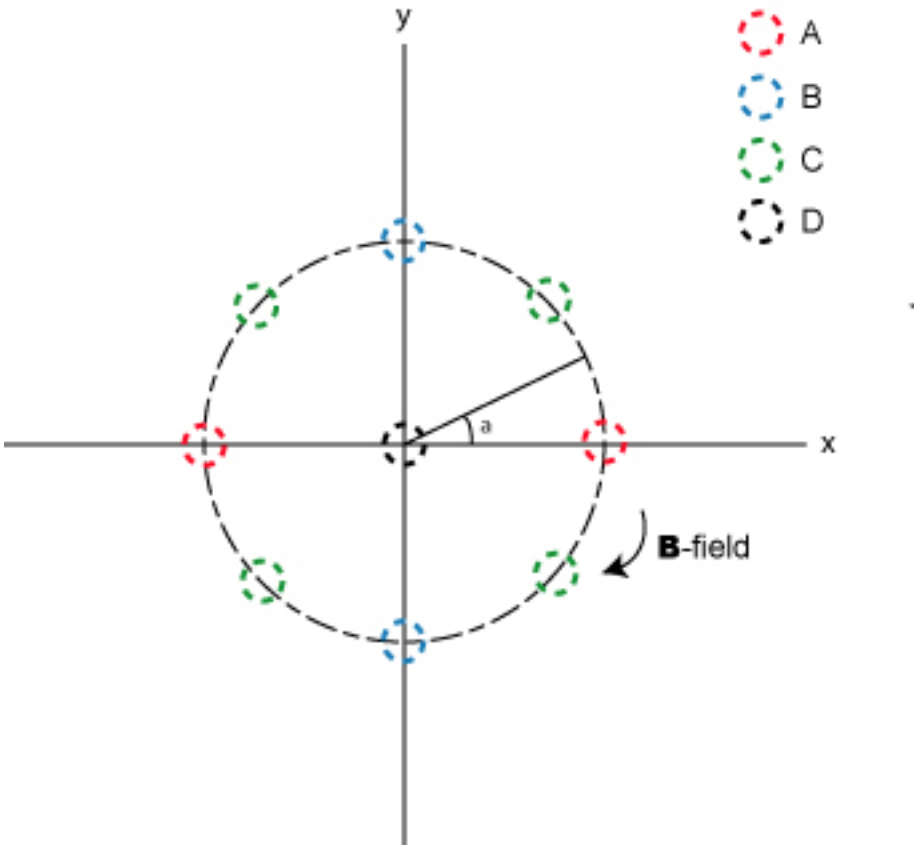

Figure 6.1: Diagram of B-fields produced at focus. The magnetic field is a loop centered $(x, y) = (0, 0)$. Small regions of interest are denoted by colored circles. At region (A), there is only magnetic field in the $\hat{y}$-direction; only in the $\hat{x}$-direction at region (B). In regions (C) (where $\alpha = n\pi/4$), the magnitude of B_x and B_y are equal. At the center, region (D), the field magnitude is zero.

no component of the magnetic field is parallel to the propagation direction of the laser. Also, there is no $\hat{z}$ component of the magnetic field because the toroidal field loop lies entirely in the plane of the target. This is suggested by particle-in-cell simulations and is a good place to start. That does not mean, however, that there is not a gradient of the magnetic field in the $\hat{z}$-direction, so $\mathbf{B}(Z) = (B_x(Z), B_y(Z), 0)$. A diagram of this is shown in figure 6.1. A few small regions of interest are denoted by colored circles. At region (A), there is only magnetic field in the $\hat{y}$-direction; only in the $\hat{x}$-direction at region (B). In regions (C), the magnitude of B_x and B_y are equal. At the center, region (D), the field magnitude is zero. Also, note that

$$B_x = B_0 \sin\alpha \tag{6.16}$$

$$B_y = B_0 \cos\alpha \tag{6.17}$$

for the reasons listed above.

Let us take the edge of the vacuum/plasma interface to be $z = 0$. The optical probe will penetrate through the plasma up to the critical surface, at $z = z_{cr}$, and then be reflected back out of the plasma. Remembering that the plasma frequency, in **cgs**, is

$$\omega_p^2 = \frac{4\pi e^2 n_e}{m_e} \tag{6.18}$$

we can rewrite the equations for W_1 and W_2 as

$$\begin{aligned} W_1 &= \int_0^{z_{cr}} \frac{a\omega_p^2}{2c\omega^3}\left(\frac{e}{m_e c}\right)^2 [B_y^2(z) - B_x^2(z)]\frac{1}{a}dz \\ &= \frac{2\pi e^4}{c^3 m_e^3 \omega^3}\int_0^{z_{cr}} n_e(z)[B_y^2(z) - B_x^2(z)]dz \end{aligned} \tag{6.19}$$

and

$$\begin{aligned} W_2 &= \int_0^{z_{cr}} -\frac{a\omega_p^2}{c\omega^3}\left(\frac{e}{m_e c}\right)^2 B_y(z)B_x(z)\frac{1}{a}dz \\ &= -\frac{2\pi e^4}{c^3 m_e^3 \omega^3}\int_0^{z_{cr}} n_e(z)B_y(z)B_x(z)dz. \end{aligned} \tag{6.20}$$

We know from both Dr. Langhoff's and Dr. Sentoku's simulations that $n_e(z)$ is fairly linear for about the first picosecond of plasma evolution. Then we can write $n_e(z) = C_n z$, where C_n is given only by the experimental conditions. For our case, $n_e(z=0) = 0$ and $n_e(z = z_{cr}) = n_{cr}$, so $C_n = n_{cr}/z_{cr}$.

We also need to know how the magnetic field changes in the $\hat{z}$-direction. But we don't know this quite yet. This information is not given in the PIC simulations. The plasma may "shield" the field similar to a high-μ material. The field could change in some really complicated way, and may extend beyond the plasma. This information may be gained from additional particle in cell simulations.

The end result depends on the 'shape' of the magnetic fields in the $\hat{z}$-direction. Additionally, there are four non-zero components of $\mathbf{M}_{jk}^{(2)}$ for our case, W_{11}, W_{12}, W_{21} and W_{22}. ($W_3 = W_{3j} = W_{i3} = 0$ because $B_z = 0$.)

In order to gain some insight in to these effects, start by considering the case where the magnetic field behaves as if $B_{x,y}(z)$ is linear in z similar to $n_e(z)$. Then

$$B_x(z) = C_{Bx} z \text{ where } C_{Bx} = \frac{B_0 \sin\alpha}{z_{cr}}, \tag{6.21}$$

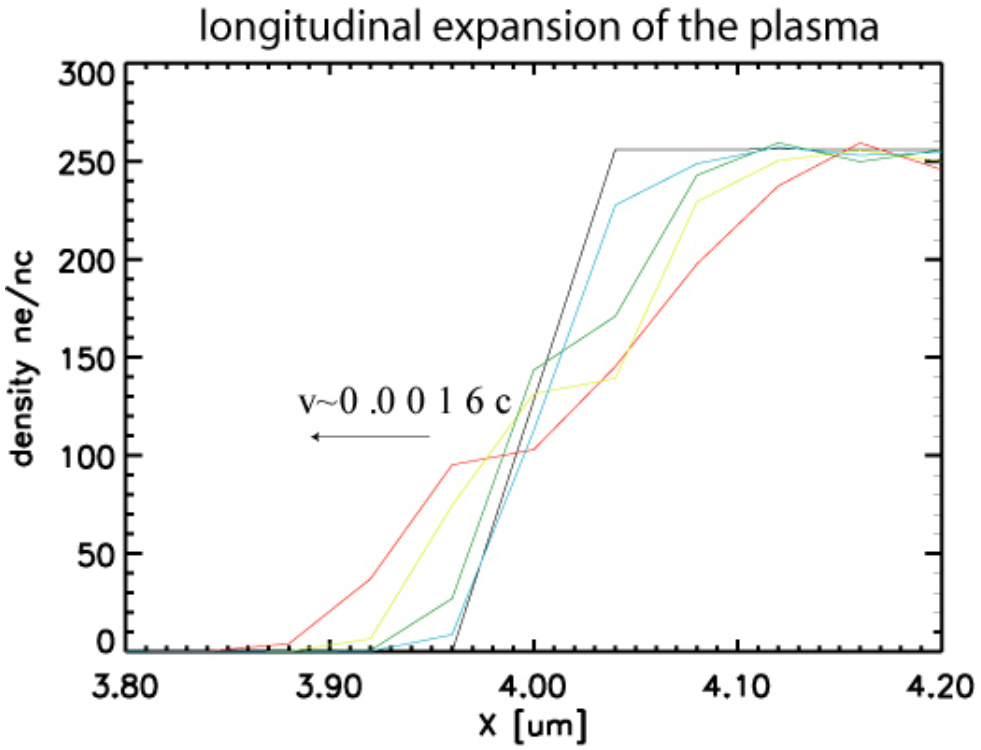

Figure 6.2: Electron density in front of the target as the heated plasma expands into vacuum at different times, as computed by particle-in-cell simulation [Y. Sentoku, Private Communication (2005)]. The simulation times are (35 fs, 70 fs, 140 fs, 210 fs, 240 fs) for the (black, blue, green, yellow, red) curves, respectively.

and

$$B_y(z) = C_{By} z \text{ where } C_{By} = \frac{B_0 \cos\alpha}{z_{cr}}. \tag{6.22}$$

In this case, the W_j and W_{jk} are

$$\begin{aligned}
W_1 &= \left(\frac{\pi e^4}{2c^3 m_e^3 \omega^3}\right) n_{cr} z_{cr} B_0^2 (\cos^2\alpha - \sin^2\alpha) && (6.23)\\
W_2 &= -\left(\frac{\pi e^4}{2c^3 m_e^3 \omega^3}\right) n_{cr} z_{cr} B_0^2 \sin\alpha\cos\alpha && (6.24)\\
W_{11} &= \frac{1}{2}\left(\frac{\pi e^4}{2c^3 m_e^3 \omega^3}\right)^2 n_{cr}^2 z_{cr}^2 B_0^4 (\cos^2\alpha - \sin^2\alpha)^2 && (6.25)\\
W_{12} &= -\frac{1}{2}\left(\frac{\pi e^4}{2c^3 m_e^3 \omega^3}\right)^2 n_{cr}^2 z_{cr}^2 B_0^4 \cos\alpha\sin\alpha(\cos^2\alpha - \sin^2\alpha) && (6.26)\\
W_{21} &= -\frac{1}{2}\left(\frac{\pi e^4}{2c^3 m_e^3 \omega^3}\right)^2 n_{cr}^2 z_{cr}^2 B_0^4 \cos\alpha\sin\alpha(\cos^2\alpha - \sin^2\alpha) && (6.27)\\
W_{22} &= \frac{1}{2}\left(\frac{\pi e^4}{2c^3 m_e^3 \omega^3}\right)^2 n_{cr}^2 z_{cr}^2 B_0^4 \cos^2\alpha\sin^2\alpha. && (6.28)
\end{aligned}$$

Note that

$$\begin{aligned}
W_{11} &= \frac{1}{2}(W_1)^2 && (6.29)\\
W_{22} &= \frac{1}{2}(W_2)^2 && (6.30)\\
W_{12} &= W_{21}. && (6.31)
\end{aligned}$$

Plug in the critical density $n_{cr} = \omega^2 m_e / 4\pi e^2$ and simplify to get

$$W_1 = \left(\frac{e^2}{2c^3 m_e^2}\right) \frac{1}{\omega} z_{cr} B_0^2 (\cos^2\alpha - \sin^2\alpha) \tag{6.32}$$

$$W_2 = -\left(\frac{e^2}{2c^3 m_e^2}\right) \frac{1}{\omega} z_{cr} B_0^2 \cos\alpha \sin\alpha \tag{6.33}$$

$$W_{11} = \frac{1}{2}\left(\frac{e^2}{2c^3 m_e^2}\right)^2 \frac{1}{\omega^2} z_{cr}^2 B_0^4 (\cos^2\alpha - \sin^2\alpha)^2 \tag{6.34}$$

$$W_{12} = -\frac{1}{2}\left(\frac{e^2}{2c^3 m_e^2}\right)^2 \frac{1}{\omega^2} z_{cr}^2 B_0^4 \cos\alpha \sin\alpha (\cos^2\alpha - \sin^2\alpha) \tag{6.35}$$

$$W_{21} = W_{12} \tag{6.36}$$

$$W_{22} = \frac{1}{2}\left(\frac{e^2}{2c^3 m_e^2}\right)^2 \frac{1}{\omega^2} z_{cr}^2 B_0^4 \cos^2\alpha \sin^2\alpha. \tag{6.37}$$

Now we are left with several equations that describe the elements of matrix M. To determine the amount of polarization rotation of the probe beam, we need to calculate $\psi = \frac{1}{2}\arctan(s_f^2/s_f^1)$. This has been done numerically for three different plasma depths $z_{cr} = [1, 5, 9]$ μm, magnetic fields 0 MG $\leqq B_0 \leqq$ 3 MG, and angles $0^\circ \leqq \alpha \leqq 90^\circ$. Plots of the results follow. In order to see small effects more clearly, we present separate plots for 0 MG $\leqq B_0 \leqq$ 1 MG and 1 MG $\leqq B_0 \leqq$ 2 MG.

We see that the polarization rotation is quite small, ranging from $< 10^{-7}$ degrees to $\sim 10^{-3}$ degrees. These rotations may be too small to measure. It is interesting that there are three areas where the rotation is zero, at $\alpha = 0^\circ$, 45°, and 90°. The rotation minimum and maximum are at $\pi/8 = 22.5^\circ$ and $3\pi/8 = 67.5^\circ$, respectively. The rotation increases as the depth of the plasma z_{cr} increases. To extend this brief analysis, I can try inputting other laser frequencies. From the matrix elements W, shorter laser frequencies should lead to larger effects. However, the polarization rotation will still be too small to be measurable without the development of fantastic new experimental techniques.

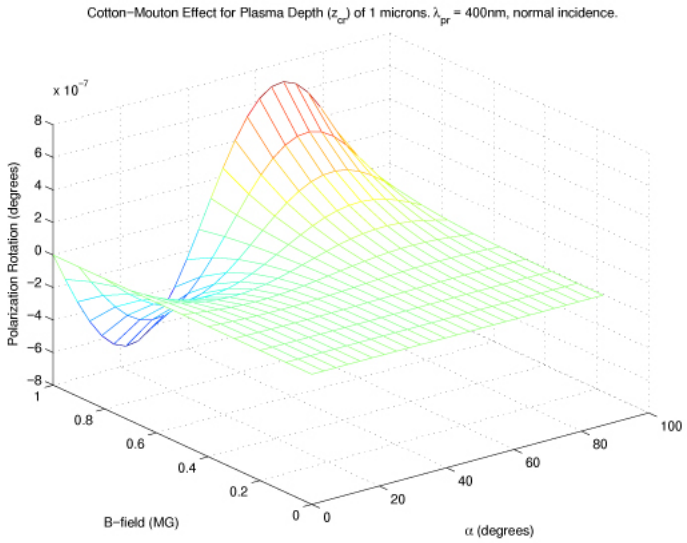

Figure 6.3: Cotton-Mouton polarization rotation for a plasma of thickness $z_{cr} = 1\mu$m, magnetic field $0 \leqq B_0 \leqq 1$ MG.

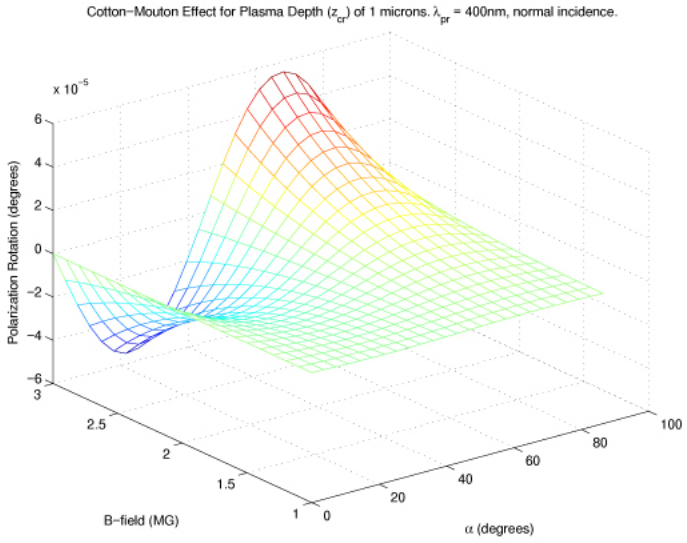

Figure 6.4: Cotton-Mouton polarization rotation for a plasma of thickness $z_{cr} = 1\mu$m, magnetic field $1 \leqq B_0 \leqq 2$ MG., and $0 \leqq \alpha \leqq 90°$.

Bibliography

[1] Max Tabak, James Hammer, Michael E. Glinsky, William L. Kruer, Scott C. Wilks, John Woodworth, E. Michael Campbell, Michael D. Perry, and Rodney J. Mason. Ignition and high gain with ultrapowerful lasers. *Physics of Plasmas*, 1(5):1626, May 1994.

[2] M. Heya, M. Nakasuji, H. Shiraga, N. Miyanaga, H. Azechi, H. Takabe, T. Yamanaka, and K. Mima. Time-resolved, two-dimensional electron-temperature distribution of laser-imploded core plasmas. *Review of Scientific Instruments*, 68(1):820, January 1997.

[3] M. Roth, T. E. Cowan, M. H. Key, S. P. Hatchett, C. Brown, W. Fountain, J. Johnson, D. M. Pennington, R. A. Snavely, S. C. Wilks, K. Yasuike, H. Ruhl, F. Pegoraro, S. V. Bulanov, E. M. Campbell, M. D. Perry, and H. Powell. Fast ignition by intense laser-accelerated proton beams. *Physical Review Letters*, 86(3):436, January 2001.

[4] R. L. Kauffman et al. High temperatures in inertial confinement fusion radiation cavities heated with 0.35 m light. *Physical Review Letters*, 73(17):2320, October 1994.

[5] R. Kodama, P. A. Norreys, K. Mima, A. E. Dangor, R. G. Evans, H. Fujita,

Y. Kitagawa, K. Krushelnick, T. Miyakoshi, N. Miyanaga, T. Norimatsu, S. J. Rose, T. Shozaki, K. Shigemori, A. Sunahara, M. Tampo, K. A. Tanaka, Y. Toyama, T. Yamanaka, and M. Zepf. Fast heating of ultrahigh-density plasma as a step towards laser fusion ignition. *Nature*, 412:798, August 2001.

[6] R. Paul Drake. *High-Energy-Density Physics: Fundamentals, Inertial Fusion, and Experimental Astrophysics*. Springer, Berlin, 2006.

[7] A. S. Sandhu, A. K. Dharmadhikari, P. P. Rajeev, G. R. Kumar, S. Sengupta, A. Das, and P. K. Kaw. Laser-generated ultrashort multimegagauss magnetic pulses in plasmas. *Physical Review Letters*, 89(22):225002, November 2002.

[8] R. J. Mason. Heating mechanisms in short-pulse laser-driven cone targets. *Physical Review Letters*, 96:035001, 2006.

[9] Y. Inubushi, T. Kai, T. Nakamura, S. Fujioka, H. Nishimura, and K. Mima. Analysis of x-ray polarization to determine the three-dimensionally anisotropic velocity distributions of hot electrons in plasma produced by ultrahigh intensity lasers. *Physical Review E*, 75:026401, February 2007.

[10] Jian Zheng, K. A. Tanaka, Y. Sentoku, A. A. Offenberger, Y. Kitagawa, R. Kodama, T. Kurahashi, K. Mima, and T. Yamanaka. Harmonic emission with cyclotron satellite structure due to strong magnetic fields produced by ultraintense laserplasma interaction. *Physics of Plasmas*, 9(8):3193 – 3196, August 2002.

[11] Y. Sentoku, H. Ruhl, K. Mima, R. Kodama, K.A. Tanaka, and Y. Kishimoto. Plasma jet formation and magnetic-field generation in the intense laser plasma under oblique incidence. *Physics of Plasmas*, 6(7):2855, 1999.

[12] Tatsufumi Nakamura, Susumu Kato, Hideo Nagatomo, and Kunioki Mima. Surface-magnetic-field and fast-electron current-layer formation by ultraintense laser irradiation. *Physical Review Letters*, 93:265002, December 2004.

[13] K. Yasuike, M. H. Key, S. P. Hatchett, R. A. Snavely, and K. B. Wharton. Hot electron diagnostic in a solid laser target by k-shell lines measurement from ultraintense laserplasma interactions (3×10^{20} w/cm^2,$\leq$ 400 j). *Review of Scientific Instruments*, 72(1):1236 – 1240, January 2001.

[14] J. W. McDonald, L. J. Suter, O. L. Landen, J. M. Foster, J. R. Celeste, J. P. Holder, E. L. Dewald, M. B. Schneider, D. E. Hinkel, R. L. Kauffman, L. J. Atherton, R. E. Bonanno, S. N. Dixit, D. C. Eder, C. A. Haynam, D. H. Kalantar, A. E. Koniges, F. D. Lee, B. J. MacGowan, K. R. Manes, D. H. Munro, J. R. Murray, M. J. Shaw, R. M. Stevenson, T. G. Parham, B. M. Van Wonterghem, R. J. Wallace, P. J. Wegner, P. K. Whitman, B. K. Young, B. A. Hammel, and E. I. Moses. Hard x-ray and hot electron environment in vacuum hohlraums at the national ignition facility. *Physics of Plasmas*, 13:032703, March 2006.

[15] Y. Sentoku, K. Mima, P. Kaw, and K. Nishikawa. Anomalous resistivity resulting from mev-electron transport in overdense plasma. *Physical Review Letters*, 90(15):155001, April 2003.

[16] S. J. Davidson, J. M. Foster, C. C. Smith, K. A. Warburton, and S. J. Rose. Investigation of the opacity of hot, dense aluminum in the region of its K edge. *Applied Physics Letters*, 52(10):847, March 1988.

[17] U. Teubner et al. Angle-dependent x-ray emission and resonance absorption

in a laser-produced plasma generated by a high intensity ultrashort pulse. *Physical Review Letters*, 70(6):794, February 1993.

[18] Y. Hironaka et al. Angular distribution of x-ray emission from a copper target irradiated with a femtosecond laser. *Applied Physics Letters*, 77(25):4110, December 2000.

[19] J. Yu, Z. Jiang, J. C. Kieffer, and A. Krol. Hard x-ray emission in high intensity femtosecond lasertarget interaction. *Physics of Plasmas*, 6(4):1318 – 1322, April 1999.

[20] L. M. Chen, P. Forget, S. Fourmaux, J. C. Kieffer, A. Krol, C. C. Chamberlain, B. X. Hou, J. Nees, and G. Mourou. Study of hard x-ray emission from intense femtosecond ti:sapphire lasersolid target interactions. *Physics of Plasmas*, 11(9):4439, September 2004.

[21] R. M. More. Electronic energy-levels in dense plasmas. *Journal of Quantitative Spectroscopy and Radiative Transfer*, 27(3):345, 1982.

[22] T. Tajima and G. Mourou. Zettawatt-exawatt lasers and their applications in ultrastrong-field physics. *Physical Review STAB*, 5:031301, 2002.

[23] T. Hall et al. Recent advances in laser-plasma experiments using foams. *Laser and Particle Beams*, 20:303, 2002.

[24] F. J. Rogers and C. A. Iglesias. Radiative atomic rosseland mean opacity tables. *Astrophysical Journal Supplement Series*, 79(2):507 – 568, April 1992.

[25] L. B. Da Silva, B. J. MacGowan, D. R. Kania, B. A. Hammel, C. A. Back, E. Hsieh, R. Doyas, C. A. Iglesias, F. J. Rogers, and R. W. Lee. Absorption

measurements demonstrating the importance of $\delta n = 0$ transitions in the opacity of iron. *Physical Review Letters*, 69(3):438 441, July 1992.

[26] O. Albert, H. Wang, D. Liu, Z. Chang, and G. Mourou. Generation of relativistic intensity pulses at a kilohertz repetition rate. *Optics Letters*, 25(15):1125, August 2000.

[27] M. C. Downer et al. Femtosecond imaging of melting and evaporation at a photoexcited silicon surface. *Journal of the Optical Society of America B*, 2(4):595, April 1985.

[28] K. H. Hong, B. Hou, J. A. Nees, E. Power, and G. A. Mourou. Generation and measurment of $> 10^8$ intensity contrast ratio in relativistic khz chirped-pulse amplified laser. *Applied Physics B*, 81:447 – 457, 2005.

[29] B. J. Pearson et al. Coherent control using adaptive learning algorithms. *Physical Review A*, 63:063412, 2001.

[30] R. A. Saroyan, D. Milam, and J. B. Trenholm. Conversion of n_2 to γ, b-integrals and laser performance figures. Interdepartmental Letter ELR - 76 - 414, Lawrence Livermore National Laboratory (LLNL), Livermore, CA, August 1976. received from G. Hays, Sep. 2004.

[31] Robert Adair, L. L. Chase, and Stephen A. Payne. Nonlinear refractive index of optical crystals. *Physical Review B*, 39:3337, February 1989.

[32] Jean-Claude Diels and Wolfgang Rudolph. *Ultrashort Laser Pulse Phenomena : Fundamentals, Techniques, and Applications on a Femtosecond Time Scale.* Optics and Photonics Series. Academic Press, San Diego, 1996. TA 1677.D54.

[33] Vitaly Krylov, Alexander Rebane, Alexander G. Kalintsev, Heinrich Schwoerer, and Urs P. Wild. Second-harmonic generation of amplified femtosecond ti:sapphire laser pulses. *Optics Letters*, 20(2):198 – 200, January 1995.

[34] Eugene Hecht. *Optics*. Addison Wesley, San Francisco, California, 4 edition, 2002.

[35] M. Born and E. Wolf. *Principles of Optics*. Cambridge University Press, seventh (expanded) edition, 1999.

[36] Ya. B. Zel'dovich and Yu. P. Raizer. *Physics of Shock Waves and High-Temperature Hydrodynamic Phenomena*. Dover, Mineola, New York, dover edition edition, 2002. One volume republication of the two-volume work originally published in English in 1966 and 1967 by Academic Press, Inc., New York.

[37] André Anders. *A formulary for plasma physics*. Akademie-Verlag Berlin, 1990.

[38] Lyman Spitzer, Jr. *Physics of Fully Ionized Gases*. Interscience Publishers, New York, 2nd edition, 1962. Library of Congress Catalog Card Number 62-18100.

[39] L. Spitzer and R. Harm. Transport phenomena in a completely ionized gas. *Physical Review*, 89(5):977, March 1953.

[40] Dimitri Mihalas and Barbara Weibel-Mihalas. *Foundations of radiation hydrodynamics*. Dover, 1999.

[41] Richard D. Hazeltine and Francois L. Waelbroeck. *The Framework of Plasma Physics*. Frontiers in Physics. Perseus Books, Reading, Mass., 1998.

[42] T. Ditmire, E. T. Gumbrell, R. A. Smith, L. Mountford, and M. H. R. Hutchinson. Supersonic ionization wave driven by radiation transport in a short-pulse laser-produced plasma. *Physical Review Letters*, 77(3):498, July 1996.

[43] W. L. Kruer. *The Physics of Laser Plasma Interactions*, volume 73 of *Frontiers in Physics*. Addison-Wesley, Redwood City, CA, 1988.

[44] S. Rosseland. Note on the absorption of radiation within a star. *Mon. Not. R. Astron. Soc.*, 84:525, May 1924.

[45] R. S. Cohen et al. The electrical conductivity of an ionized gas. *Physical Review*, 80(2):230, October 1950.

[46] J. Delettrez. Thermal electron transport in direct-drive laser fusion. *Can. J. Phys.*, 64:932, 1986.

[47] J. M. Wallace. Nonlocal energy deposition in high-intensity laser-plasma interactions. *Physical Review Letters*, 55(7):707, August 1985.

[48] K. Estabrook and W. L. Kruer. Properties of resonantly heated electron distributions. *Physical Review Letters*, 40(1):42, January 1978.

[49] P. Gibbon and A. R. Bell. Collisionless absorption in sharp-edged plasmas. *Physical Review Letters*, 68(10):1535, March 1992.

[50] O. L. Landen et al. Measurement of the expansion of picosecond laser-produced plasmas using resonance absorption profile spectroscopy. *Physical Review Letters*, 63(14):1475, October 1989.

[51] Michael P. Marder. *Condensed Matter Physics*. John Wiley & Sons, corrected edition, 2000.

[52] Bradley W. Carroll and Dale A. Ostlie. *An Introduction To Modern Astrophysics*. Addison-Wesley, 1996.

[53] Ronnie Shepherd, P. Audebert, C. Chenais-Popovics, J. P. Geindre, M. Fajardo, C. Iglesias, S. Moon, F. Rogers, J. C. Gauthier, and P. Springer. Absorption of bound states in hot, dense matter. *Journal of Quantitative Spectroscopy and Radiative Transfer*, 71(2 - 6):711 – 719, October 2001.

[54] T. S. Perry, S. J. Davidson, F. J. D. Serduke, D. R. Bach, C. C. Smith, J. M. Foster, R. J. Doyas, R. A. Ward, C. A. Iglesias, F. J. Rogers, J. Abdallah, Jr., R. E. Stewart, R. J. Wallace, J. D. Kilkenny, and R. W. Lee. Opacity measurements in a hot dense medium. *Astrophysical Journal Supplement Series*, 127(2):433 436, April 2000.

[55] T. D. Donnelly et al. Hard x-ray and hot electron production from intense laser irradiation of wavelength-scale particles. *Journal of Physiscs B: Atomic, Molecular and Optical Physics*, 34:L313, 2001.

[56] N. A. Ebrahim et al. Energy deposition by hot electrons in CO^2-laser-irradiated targets. *Physical Review A*, 25(4):2440, April 1982.

[57] N. A. Ebrahim et al. Anomalous energy transport to rear surface of microdisks at high laser irradiances. *Physical Review Letters*, 43(27):1995, December 1979.

[58] J. C. Keiffer, H. Pépin, M. Piché, J. P. Matte, T. W. Johnston, P. Lavigne, and F. Martin. Hot-electron energy deposition in CO^2-laser-irradiated targets consistent with magnetic-field-induced surface transport. *Physical Review Letters*, 50(14):1054, April 1983.

[59] W. Priedhorsky et al. Hard-x-ray measurements of 10.6-m laser-irradiated targets. *Physical Review Letters*, 47(23):1661, December 1981.

[60] S. C. Wilks. Simulations of ultraintense laser-plasma interactions. *Physics of Fluids B*, 5(7):2603, July 1993.

[61] L Gremillet et al. Time-resolved observation of ultrahigh intensity laser-produced electron jets propagating through transparent solid targets. *Physical Review Letters*, 83(24):5015, December 1999.

[62] D. W. Forslund and J. U. Brackbill. Magnetic-field-induced surface transport on laser-irradiated foils. *Physical Review Letters*, 48(23):1614, June 1982.

[63] Y. Sentoku, K. Mima, Z. M. Sheng, P. Kaw, K. Nishihara, and K. Nishikawa. Three-dimensional particle-in-cell simulations of energetic electron generation and transport with relativistic laser pulses in overdense plasmas. *Physical Review E*, 65:046408, 2002.

[64] K. Mima. Private communication. Notes on electron fountain., June 2004.

[65] J. D. Jackson. *Classical Electrodynamics*. John Wiley and Sons, New York, second edition, 1975.

[66] Hans R. Griem. *Plasma Spectroscopy*. McGraw-Hill, New York, 1964. Library of Congress Catalog Card Number 63-23250.

[67] Francis F. Chen. *Introduction to Plasma Physics and Controlled Fusion: Plasma Physics*, volume v.1: Plasma Physics. Plenum, NY, NY, 2nd edition, 1984.

[68] Bixue Hou, John A. Nees, Wolfgang Theobald, Gérard A. Mourou, L. M. Chen, Jean-Claude Kieffer, Andrzej Krol, and C. C. Chamberlain. Dependence of

hard x-ray yield on laser pulse parameters in the wavelength-cubed regime. *Applied Physics Letters*, 84(13):2259, March 2004.

[69] B. T. Bowes, H. Langhoff, M. C. Downer, M. Wilcox, B. Hou, J. Nees, and G. Mourou. Femtosecond microscopy of radial energy transport in a micrometer-scale aluminum plasma excited at relativistic intensity. *Optics Letters*, 31(1):116, January 2006.

[70] National Institutes of Health. Imagej: Image processing and analysis in java. http://rsb.info.nih.gov/ij/.

[71] H. Langhoff. Private communication. Notes on energy transport., 2005.

[72] H. Langhoff. Private communication. Notes on energy transport., 2006.

[73] H. Langhoff. Private communication. Notes on energy transport., 2004.

[74] W. Rozmus et al. A model of ultrashort laser pulse absorption in solid targets. *Physics of Plasmas*, 3(1):360, January 1996.

[75] F. Alouani Bibi and J. P. Matte. Influence of the electron distribution function shape on nonlocal electron heat transport in laser-heated plasmas. *Physical Review E*, 66:066414, 2002.

[76] J. C. Kieffer et al. Short-pulse laser absorption in very steep plasma density gradients. *Physical Review Letters*, 62(7):760, February 1989.

[77] S. Kato et al. Wave breaking and absorption efficiency for short pulse p-polarized laser light in a very steep density gradient. *Physics of Fluids B*, 5(2):564, February 1993.

[78] D. F. Price et al. Absorption of ultrashort laser pulses by solid targets heated rapidly to temperatures 11000 ev. *Physical Review Letters*, 75(2):252, July 1995.

[79] D. Fisher, M. Fraenkel, Z. Henis, E. Moshe, and S. Eliezer. Interband and intraband (drude) contributions to femtosecond laser absorption in aluminum. *Physical Review E*, 65:016409, 2002.

[80] B. Rethfeld, A. Kaiser, M. Vicanek, and G. Simon. Ultrafast dynamics of nonequilibrium electrons in metals under femtosecond laser irradiation. *Physical Review B*, 65:214303, 2002.

[81] S. Kato, R. Kawakami, and K. Mima. Nonlinear inverse bremsstrahlung in solid-density plasmas. *Physical Review A*, 43(10):5560, May 1991.

[82] Y. Horovitz, S. Eliezer, A. Ludmirsky, Z. Henis, E. Moshe, R. Shpitalnik, and B. Arad. Measurements of inverse faraday effect and absorption of circularly polarized laser light in plasmas. *Physical Review Letters*, 78(9):1707 1710, March 1997.

[83] M. K. Grimes et al. Experimental identification of "vacuum heating" at femtosecond-laser-irradiated metal surfaces. *Physical Review Letters*, 82(20):4010, May 1999.

[84] R. C. Elton. *X-Ray Lasers*. Academic Press, Boston, 1990.

[85] R. L. Kelly. *Atomic and ionic spectrum lines below 2000 angstroms : hydrogen through krypton*. Journal of physical and chemical reference data. V. 16 Supplements 1-3. American Chemical Society and the American Institute of Physics for the National Bureau of Standards, New York, 1987.

[86] E. Nardi and Z. Zinamon. Radiative opacity of high-temperature and high-density gold. *Physical Review A*, 20(2):1197, September 1979.

[87] C. Constantin, C. A. Back, K. B. Fournier, G. Gregori, O. L. Landen, S. H. Glenzer, E. L. Dewald, and M. C. Miller. Supersonic propagation of ionization waves in an underdense, laser-produced plasma. *Physics of Plasmas*, 12:063104, June 2005.

[88] P. A. Holstein, J. Delettrez, S. Skupsky, and J. P. Matte. Modeling nonlocal heat flow in laser-produced plasmas. *Journal of Applied Physics*, 60(7):2296, October 1986.

[89] A. V. Brantov, V. Yu. Bychenkov, and V. K. Tikhonchuk. Absorption of a short pulse of laser radiation in a high-density plasma. *Plasma Physics Reports (Fizika Plazmy)*, 24(4):325, 1998.

[90] P. Mora and R. Pellat. Self-similar expansion of a plasma into a vacuum. *Physics of Fluids*, 22(12):2300 – 2304, December 1979.

[91] R. Ramis et al. Multi-a computer code for one-dimensional multigroup radiation hydrodynamics. *Computer Physics Communications*, 49:475, 1988.

[92] J. P. Christiansen, D. E. T. F. Ashby, and K. V. Roberts. Medusa a one-dimensional laser fusion code. *Computer Physics Communications*, 7:271, 1974.

[93] Y. T. Lee and R. M. More. An electron conductivity model for dense plasmas. *Physics of Fluids*, 27(5):1273, May 1984.

[94] Joseph W. Goodman. *Introduction to Fourier Optics*. McGraw-Hill Series in

Electrical and Computer Engineering. McGraw-Hill, Boston, second edition, 1996.

[95] M. Becker. Class notes from EE383P – Fourier Optics, 2003.

[96] Y. Sentoku. Private communication. PIC Simulations, November 2005.

[97] N. H. Matlis, S. Reed, S. S. Bulanov, V. Chvykov, T. Matsuoka G. Kalintchenko, P. Rousseau, V. Yanovsky, A. Maksimchuk, S. Kalmykov, G. Shvets, and M. C. Downer. Snapshots of laser wakefields. *Nature Physics*, 2:749 – 753, 2006.

[98] G. Dattoli and S. E. Segre. Evaluation of the polarimetric transition matrix for a magnetized plasma. *Physics of Plasmas*, 4(3):898 – 900, March 1997.

[99] Ch. Fuchs and H. J. Hartfuss. Line integrated density measurements based on CottonMouton polarimetry. *Review of Scientific Instruments*, 70(1):722 – 725, January 1999.

[100] K. Guenther and JET-EFDA Contributors. Approximate method to extract the pure Faraday and CottonMouton effects from polarimetry measurements in a tokamak. *Plasma Physics and Controlled Fusion*, 46:1423 – 1441, September 2004.

[101] J. O'Rourke. On the measurement of the poloidal magnetic field in a large tokamak. *Plasma Physics and Controlled Fusion*, 26(9):1139 – 1140, September 1984.

[102] S. E. Segre. The measurement of poloidal magnetic field in a tokamak by the change of polarization of an electromagnetic wave. *Plasma Physics*, 20(4):295 – 307, April 1978.

[103] Ch. Fuchs and H. J. Hartfuss. Cotton-Mouton effect measurement in a plasma at the W7-AS stellarator. *Physical Review Letters*, 81(8):1626 1629, August 1998.

[104] S. E. Segre. Plasma polarimetry for large cottonmouton and faraday effects. *Physics of Plasmas*, 2(8):2908 – 2914, August 1995.

[105] C. H. Ma, D. P. Hutchinson, and K. L. Vander Sluis. A modulated submillimeter-laser polarimeter for the measurement of the Faraday rotation by a plasma. *Applied Physics Letters*, 34(3):218 – 220, February 1979.

[106] Sergio E. Segre. Evolution of the polarization state for radiation propagating in a nonuniform, birefringent, optically active, and dichroic medium:the case of a magnetized plasma. *Journal of the Optical Society of America A*, 17(1):95 – 100, January 2000.

[107] S.E. Segre. A review of plasma polarimetry - theory and methods. *Plasma Physics and Controlled Fusion*, 41(2):R57 – 100, February 1999.

[108] Prof. Richard Fitzpatrick. Faraday rotation. web; http://farside.ph.utexas.edu/teaching/em/lectures/node101.html.

Vita

Benjamin Bowes was born in Jackson, Michigan, USA on June 2, 1977 to Kerry and Thomas Bowes. While growing up his family moved frequently around the state of Michigan. Benjamin graduated from Cadillac Senior High School in Cadillac, Michigan in June, 1995. From there he journeyed to Ann Arbor, Michigan to attend the University of Michigan. At Michigan he double-majored in Physics and Astronomy. During this time he worked as an undergraduate research assistant in the Astronomy and Physics departments. He graduated from the University of Michigan in May, 2000 with high departmental honors in Physics. In August, 2000, Benjamin moved to Austin, Texas, and began graduate study in Physics at the University of Texas at Austin. He joined the lab of Prof. M. Downer in January, 2001.

Permanent Address: c/o: Kerry and Thomas Bowes

603 Pine Street

PO Box 306

Elk Rapids, Michigan 49629

This dissertation was typeset with LaTeX 2_ε[1] by the author.

[1] LaTeX 2_ε is an extension of LaTeX. LaTeX is a collection of macros for TeX. TeX is a trademark of

the American Mathematical Society. The macros used in formatting this dissertation were written by Dinesh Das, Department of Computer Sciences, The University of Texas at Austin, and extended by Bert Kay, James A. Bednar, and Ayman El-Khashab.